J. Mech. Phys. Solids 160 (2022) 104740

Contents lists available at ScienceDirect

Journal of the Mechanics and Physics of Solids

journal homepage: www.elsevier.com/locate/jmps

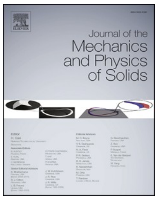

Exploiting interface patterning for adhesion control

Ranny R. Zhao, Kevin T. Turner, John L. Bassani *

Mechanical Engineering and Applied Mechanics Department, University of Pennsylvania, 220 S. 33rd Street, Philadelphia, PA 19104, United States of America

ARTICLE INFO

Keywords:
Imperfect adhesion
Traction-separation relation
Cohesive zone model
Interface topography
Finite element analysis

ABSTRACT

Surface force-mediated adhesion, e.g. via van der Waals forces, is critical for direct bonding of bulk solids in the absence of chemical bonding or an adhesive layer. However, no two surfaces are ideally flat or perfectly *conformal* due to surface roughness or intentional patterning. When adhered, non-zero surface tractions arise wherever the local separation of the interface differs from its intrinsic equilibrium separation, inducing regions of tensile and compressive stresses. A fundamental understanding of such imperfect adhesion is important and unlocks opportunities to control interfacial strength and toughness in various applications including MEMS/NEMS, micro-transfer printing, and processes to manufacture advanced 3D integrated-circuits. This paper investigates the fundamentals of direct adhesion of *non-conformal* surfaces by examining the interplay of the (i) intrinsic traction-separation relation (TSR), (ii) interface topography, and (iii) elastic properties of the adhered bodies. The TSR adopted accounts for strong repulsion when the interface separation is less than the equilibrium separation, and only the normal surface tractions are considered. The effective TSR properties, including the overall adhesion strength and work of separation, are determined from numerical calculations. Simple closed-form solutions are obtained for rigid bulk solids. A finite element model utilizing cohesive elements in a periodic cell is constructed to study cases with non-uniform deformation in the elastic solids.

1. Introduction

This work investigates surface-force mediated adhesion, i.e., direct bonding via van der Waals forces (Israelachvili, 2011; Maugis, 2013), between bulk solids with an engineered surface pattern with its height on the length scale of the range of surface forces. There have been many studies of adhesion and fracture of *conformal* interfaces (i.e. with nominally uniform gaps throughout, filled by an adhesive, or closed by inelastic deformation) as well as contact problems involving indenters and asperities (Johnson, 1985; Maugis, 2013). Nevertheless, there remains an incomplete understanding of imperfect adhesion of *non-conformal* interfaces. A fundamental understanding of imperfect adhesion is needed to unlock opportunities to control interfacial strength and toughness in a wide range of applications, including MEMS/NEMS, micro-transfer printing, manufacturing processes for advanced integrated-circuits, biomedical devices, and soft robotics.

The effect of fine-scale surface roughness on adhesion has been studied over many decades, including recent studies of roughness in a fractal sense, leading to relationships between roughness and apparent work of adhesion (Fuller and Tabor, 1975; Pastewka and Robbins, 2014; Persson, 2014). In contrast, the role of patterned surfaces with feature height comparable to the range of surface forces on adhesion of elastic solids has received much less attention. This is surprising, since engineered surface patterns can be precisely

---

* Corresponding author
E-mail address: bassani@seas.upenn.edu (J.L. Bassani).

https://doi.org/10.1016/j.jmps.2021.104740
Received 1 September 2021; Accepted 2 December 2021

patterned via lithography and etching and bonded as part of semiconductor manufacturing processes. For example, shallow etches ($\sim 1\mu$m deep) have been used to prevent local adhesion in direct wafer bonding and lead to control of stable bond propagation (Turner and Spearing, 2002, 2006). Indeed, engineered patterned interfaces offer a route for the deterministic control of adhesion resulting from direct bonding for many technologies.

Interfaces with periodic patterns can be categorized as *conformal* and *non-conformal* interfaces, where the former has been more widely studied. For example, inspired by periodic suture joints in nature, there have been several investigations of the influence of *conformally* patterned interfaces on adhesion strength and effective toughness. Among c*onformal* periodic triangular, rectangular, and trapezoidal interface patterns, slender triangles were found to be the optimal geometry for achieving high stiffness, strength, and toughness due to a relatively uniform distribution of stresses (Li et al., 2011, 2013; Lin et al., 2014). Others have used cohesive zone models to investigate the effects of sinusoidal patterns and patterns with arbitrary kink angles on effective toughness under far-field Mode I conditions (Zavattieri et al., 2007; Cordisco et al., 2012, 2016; Hosseini et al., 2019); in general, *conformal* patterns with relatively high aspect ratios are found to significantly affect the effective toughness for both similar and dissimilar adhered elastic bodies.

Studies that have adopted cohesive zone models of fracture of flat or *conformally* patterned interfaces have not addressed the strong repulsion at very close separations as a function of the underlying traction-separation relation, either because the tractions tend to be tensile everywhere across the interface or for repulsive interactions (compressive tractions) the interaction is treated as a classical contact problem. In fact, many studies only account for finite repulsive tractions when the interface separation becomes less than an equilibrium separation (Zavattieri et al., 2007), which is the case for the traction-separation relation resulting from the so-called universal binding energy of Rose et al. (1981) that was adopted by Xu and Needleman's (1993) (see also Tvergaard and Hutchinson, 1993; Wu et al., 2016, 2019; Hosseini et al., 2019). In contrast, the traction-separation relation that results from Lennard-Jones interactions between two semi-infinite bodies leads to repulsive tractions that blow up as the negative 9th power of the separation. As will be shown in this investigation of direct bonding of *non-conformally* patterned surfaces, accounting for a strong repulsion is essential, particularly for the equilibrium configuration in the absence of applied loads. We have proposed a phenomenological traction-separation relation that meets this requirement.

As already noted, less well studied is the direct bonding of engineered *non-conformal* interfaces, which is fundamentally different than the direct bonding of *conformal* interfaces. In a *non-conformal* interface, regions where the separation of two solids is not at the ideal equilibrium separation (zero traction), details of adhesive interactions can have significant effects (Springman and Bassani, 2008; Ciavarella et al., 2017) and lead to spatially-varying interface tractions, e.g. over separations of tens of nanometers or less. In fact, the extension of Hertz spherical contact problem with adhesion can be appropriately considered as a *non-conformal* interface in the mechanics of imperfect adhesion. Both Bradley (1932) and Derjaguin (1934) proposed models for the adhesion of rigid spheres, in which they both considered the attractive and repulsive part of interaction potential and that the interaction stresses over the curved bodies provided the adhesive interaction force (Barthel, 2008). Later, models for adhesion of spheres in contact were developed considering from rigid bodies (DMT theory) to very soft elastic bodies (JKR theory) (Johnson et al., 1971; Derjaguin et al., 1975; Barthel, 2008). More recently, the work of Turner and Spearing (2002,2006) on the effect of wafer bow and etched patterns on direct wafer bonding

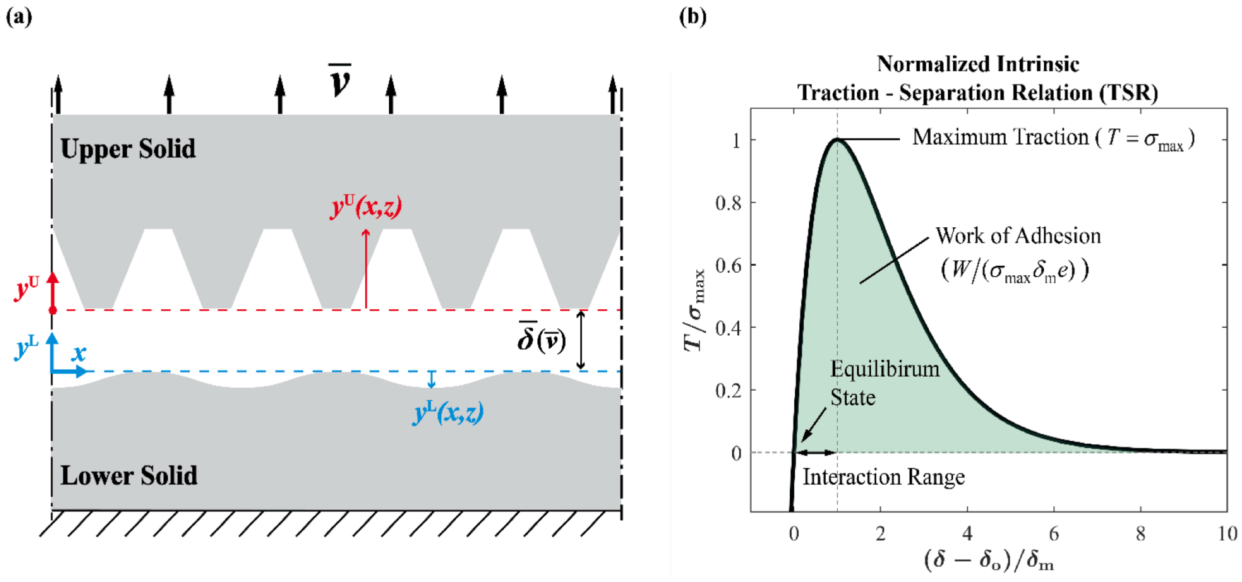

Fig. 1. (a) 2D schematic of generally patterned bulk solids adhered through surface forces acting across the interface. The horizontal dash lines correspond to the bounding planes that are introduced in to define the surface topographies (see Section 3). (b) The normalized intrinsic traction-separation relation (TSR) corresponds to the interaction between ideally flat surfaces, where the traction-free equilibrium separation is δ_o, the interaction range characterized from $T = 0$ to $\sigma_{\max}$ is δ_m, and the work of adhesion, W, is the area under the TSR for $\delta_o \le \delta < \infty$.

and Springman and Bassani (2008, 2009) on adhesion of thin shells to a rigid substrate both considered direct bonding of *non-conformal* surfaces and suggested the possibility to use patterning to control adhesion.

Imperfect adhesion arises from direct bonding of *non-conformal* surfaces wherever the separation of the surfaces in the adhered state differs from an equilibrium separation, δ_o, at which surface tractions vanish, $T(\delta_o) = 0$. Although deformation of the surfaces can increase coherence by reaching more intimate contact, in general, the perfect bonding condition cannot be met everywhere in the equilibrium configurations (i.e. no external load) that correspond to a minimum in both the local and the total free energy of the system. From a microscopic perspective of a *non-conformally* patterned interface (sketched in Fig. 1a), the intrinsic traction-separation relation (TSR) shown in Fig. 1b describes the interaction between the two adhered solids locally, with the equilibrium configuration defined by the absence of externally applied loads. The interface separation depends on both the relative position of solid surfaces, as well as the local displacements that take place in the deformable solids near the interface. As a result, there will be non-zero tractions distributed over the entire adhered region, resulting in a fracture energy that is less than the ideal work of adhesion, W. Even at overall equilibrium, adhesion between the *non-conformal* surfaces leads to regions of both tensile and compressive tractions (Springman and Bassani, 2008; Pastewka and Robbins, 2014). The combination of these factors will result in an effective TSR that depends on the geometry of the patterned interface as well as deformations in the elastic bulk solids. Effective properties are associated with the averages over the adhering surfaces, which includes the overall work of separation $\overline{W}$, the effective interfacial adhesive strength $\overline{T}_{\max}$, the effective equilibrium separation $\overline{\delta}_{\mathrm{eq}}$, and the effective interaction range $\overline{\delta}_{\mathrm{m}}$. In addition, the effective fracture toughness of a patterned interfaces generally depends on the loading configuration, e.g. the combination of far-field tension and shear (Xia et al., 2013, 2015; Hossain et al., 2014). In the regime of adhesion where the details of bonding, i.e. the details of the TSR, can be ignored, a Griffith-type approach is valid for computing W(Turner and Spearing, 2002, 2006; Springman and Bassani, 2008). This analogy reveals the strong dependence of the fracture stress on the geometry of patterned interfacial features.

The interface pattern geometry together with the highly nonlinear nature of the cohesive traction-separation relation generally lead to highly non-uniform fields across a *non-conformally* patterned interface. We find that several dimensionless ratios must be considered such that the surface topography dimensions are considered relative to the TSR properties. The overall goal of this paper is to provide a framework to understand imperfect adhesion, leading to analytically-based design principles for surface force-mediated adhesion of *non-conformal* interfaces associated with engineered patterns. The interplay between intrinsic adhesive properties (TSR; Section 2), interface geometry (Secs. 3 and Secs. 4), and bulk material elastic deformation (Section 5) on the effective TSR is investigated through calculations of the separation of periodically patterned interfaces. In this work, only tractions acting normal to the interface plane are considered.

2. Interface traction-separation relation (TSR)

This work is concerned with surface-force mediated direct adhesion, e.g. van der Waals forces, between bulk solids. Only forces acting normal to the surfaces, i.e. normal tractions, are considered. If the normal separation δ between surfaces of bulk solids is approximately in the $1 \sim 100\,\mathrm{nm}$ range, adhesive interactions can arise with varying strength that depend on both the materials and the separation of those surfaces. In the absence of strong bonding (e.g., covalent, ionic or metallic), relatively long-range van der Waals weak attractive interactions and possibly slightly stronger hydrogen bonding come into play (Na et al., 2016). If the separation is very small, e.g. in the sub-nanometer range, strong repulsion arises. Those interactions can be defined locally in terms of a relationship between the surface separation and the resulting traction (dimension of force per unit area). Classical investigations of these interactions are found in the work of Tabor and Israelachvili (Tabor and Winterton, 1968; Israelachvili and Tabor, 1972; Israelachvili, 1974, 2011) and their mechanics implications in the work of Maugis (2013) and many others. Equilibrium configurations defined by the absence of externally applied forces are associated with the as fabricated system.

Two different configurations are imagined. The first is simply two rectangular blocks interacting across ideally flat surfaces, in which case the adhesive tractions vanish at the equilibrium separation, δ_o, and its traction-separation relation is referred to as the intrinsic TSR. As the blocks are pulled apart from the equilibrium state, a characteristic response arises: an attractive traction increases with separation up to some maximum value then decreases monotonically with increasing separation, eventually becoming negligible. For weak interaction, e.g. van der Waals, the energy per unit area to fully separate those solid blocks with ideally flat surfaces is referred to as the work of adhesion, W, with values in the range of $10^{-3} \sim 1\,\mathrm{J/m^2}$, where the higher values are associated with hydrogen bonding (Gao and Yao, 2004; Israelachvili, 2011; Maugis, 2013; Na et al., 2016). In a given material system, for two reasons, the TSR is essentially phenomenological in nature since, as discussed by Israelachvili (1974, 2011): i) different types of molecular interactions, including many-body interactions, lead to different long-range attractive interactions and ii) repulsive interactions as atoms are pushed together involve nearly intractable quantum mechanical problems. Perhaps one of the most widely adopted TSR is based upon Lennard-Jones interactions between all atoms in two half-spaces, which leads to surface tractions that depend additively on the separation to the -3 and -9 powers (Springman and Bassani, 2008; Maugis, 2013); the $(\delta_o/\delta)^9$ term gives rise to strong repulsion that is essentially phenomenological in nature. Furthermore, that TSR involves only 2 constants, which limits fitting to basic material parameters including the equilibrium separation, elastic modulus, maximum traction, and work of adhesion.

The second is a class of configurations involving non-flat surfaces, such as patterned surfaces and rough surfaces (Turner and Spearing, 2002, 2006; Springman and Bassani, 2008; Tvergaard and Hutchinson, 2009; Menga et al., 2016), which are the subject of this paper. In these cases, the equilibrium state involves non-zero surface tractions with a zero resultant (average), and therefore include both attractive and repulsive tractions. Given local surface interactions governed by a TSR, effective TSR properties are determined by solutions to problems involving the external loads applied to bulk solids interacting across the non-flat surfaces and generally include effects of bulk straining.

We consider only normal traction (T) – normal separation (δ) interactions, neglecting shear tractions between interacting surfaces. The TSR characterizes local interactions across perfectly flat surfaces between bulk solids with characteristics that include the equilibrium separation, δ_o, where δ_o is on the order of and typically greater than nearest neighbor atomic spacing (Na et al., 2016), the maximum traction $\sigma_{\max} = T(\delta_o + \delta_m)$, where δ_m is a measure of the range of interactions, and the work of adhesion $W = \int_{\delta_o}^{\infty} T d\delta$. Furthermore, regarding δ as a measure of atomic separation, we assume that the magnitude of the repulsive traction becomes infinite as $\delta \to 0$.

Various analytical forms for the TSR have been proposed which all are essentially phenomenological in nature (Rose et al., 1981; Needleman, 1990; Xu and Needleman, 1993; Israelachvili, 2011; Park and Paulino, 2011; Maugis, 2013;). Given various analytical forms for the TSR, there also have been a number of experimental studies to extract TSR parameters, both direct and iterative methods (Guo et al., 1999; Bažant, 2001; Hong and Kim, 2003; Jeong et al., 2009; Gowrishankar et al., 2012; Na et al., 2016; Wu et al., 2019). Among the many analytical forms for phenomenological TSR laws that have been proposed and widely adopted, the aforementioned Lennard-Jones 3–9 law, which only involves 2 parameters, and the universal binding energy function of Rose-Ferrante-Smith, which involves 3 parameters, have motivated the form of 4-parameter TSR (Fig. 1b) we have proposed in this investigation:

$$T(\delta) = \frac{\psi}{\beta}\left[1 + \alpha\left(\frac{\beta}{\delta}\right)\right]\left(\frac{\delta - \delta_o}{\beta}\right)\exp\left(-\frac{\delta - \delta_o}{\beta}\right) \tag{1}$$

where δ_o is the equilibrium separation, i.e. $T(\delta_o) = 0$, β characterizes the range of interactions, the term multiplying $\alpha > 0$ accounts for strong repulsion for $\delta < \delta_o$, and ψ has units of energy per unit area. An even stronger repulsion can be easily included by raising the term (β/δ) multiplying α to an arbitrary power greater than one (e.g., 12 in the Lennard-Jones case). The Rose-Ferrante-Smith TSR corresponds to $\alpha = 0$, in which case straightforward calculations give (corresponding quantities denoted with a tilde) the work of adhesion $\widetilde{W} = \psi$, the maximum traction $\widetilde{\sigma}_{\max} = \psi/(e\beta)$ at an interaction range $\widetilde{\delta}_m \equiv \delta - \delta_o = \beta$, where $e = \exp(1)$, and the interface stiffness (modulus) $\widetilde{E} \equiv dT/d(\delta/\delta_o)|_{\delta=\delta_o} = \psi/\beta^2 = \widetilde{\sigma}_{\max} e/\beta$. For small values of α, e.g. $\alpha = 0.01$ which is adopted for the results presented below, values of W, $\sigma_{\max}$, δ_m and E given the parameters ψ, δ_o, β and α in (1), are not too different than those for $\alpha = 0$. The potential associated with (1) as well as accurate approximations of W, $\sigma_{\max}$, δ_m and E for small α are given in the Appendix A. As noted above, the Rose-Ferrante-Smith TSR ($\alpha = 0$) only accounts for weak finite repulsive interaction $T(\delta = 0) = -(\psi\delta_o/\beta^2)\exp(\delta_o/\beta)$ as $\delta \to 0$, which would allow for material interpenetration under finite compressive tractions, while for any $\alpha > 0$, (1) yields $T \to -\infty$ as $\delta \to 0$. This is an important consideration for equilibrium configurations corresponding to vanishing average traction for *non-conformally* patterned surfaces.

3. Adhesion of *non-conforming* surfaces

Consider two bulk solids interacting across an interface, with the surface topographies of each solid varying on the length scales sufficiently greater than the atomic scales that determine van der Waals forces (Barthel, 2008; Maugis, 2013). In the absence of surface tractions, the unstressed (as fabricated) surface geometries of the upper and lower solids (denoted with superscripts U and L, respectively) are defined relative to the $x - z$ bounding planes ($y =$ constant planes), such that the surface of the upper bulk solid is $y_o^U(x,z) \geq 0$ with $\min_{x,z} y_o^U(x,z) = 0$ and the surface of the lower bulk solid is $y_o^L(x,z) \leq 0$ with $\max_{x,z} y_o^U(x,z) = 0$ as depicted in Fig. 1a. Bulk deformations arising from both interface traction forces and applied external loads cause those surfaces to deform, and similar representations define $y^U(x,z) \geq 0$ with $\min_{x,z} y^U(x,z) = 0$ and $y^L(x,z) \leq 0$ with $\max_{x,z} y^U(x,z) = 0$. Note that the bounding planes generally evolve with external loading. Therefore, the gap between the upper and lower surfaces across the interface at any state of deformation can be represented as:

$$\delta(x,z) = y^U(x,z) + y^L(x,z) + \overline{\delta} \tag{2}$$

where $\overline{\delta}$ is the separation between the bounding planes that define y^U and y^L. Each of the 3 terms on the right-hand side of (2), in general, vary with applied loads on the bimaterial system. The resulting interface tractions are assumed to act only in the $y-$ direction, i.e. the traction vector acting on those surfaces is $\mathbf{T} = T\mathbf{e}_y$, where $\mathbf{e}_y$ is the unit vector in the $y-$ direction (normal to $x - z$ planes). Under specified external loading and the unknown surface tractions, the interface separation (2) is determined from solutions to a governing boundary-value problem that is highly nonlinear even for linearly elastic bulk material behavior. The unknown equilibrium state is defined in the absence of applied loads.

Surface deformations, which arise from both interface tractions and externally applied loads, are determined from solutions of the governing equations of equilibrium, compatibility, and constitutive relations. From the equilibrium state, i.e. the reference configuration, consider a uniform vertical displacement $\overline{v}$ applied to the top surface ($y =$ constant) of the upper bulk solid, with the bottom surface of the lower bulk solid (also $y =$ constant) held fixed. Both top and bottom external surfaces and the interface have $\sigma_{yx} = \sigma_{yz} = 0$. All other external surfaces subjected to periodic boundary conditions (see Fig. 1a). The separation, $\overline{\delta}$, of the interface bounding planes, as well as y^U and y^L in the case of compliant bulk materials, depend on $\overline{v}$, but the relations may not be one-to-one because of spring back due to the bulk elastic deformation as discussed below in Section 5. In general, for *non-conforming* surfaces, the bulk solids in the reference equilibrium state $\overline{\delta} = \overline{\delta}_{eq}$ is stressed, and for rigid bulk solids, $\overline{\delta} = \overline{v}$. Of course, more general external loading conditions can be considered. Only for perfectly *conforming* surfaces ($y^{\mathrm{U}} + y^{\mathrm{L}} = \text{constant}$), which includes perfectly flat surfaces ($y^{\mathrm{U}} = 0 = y^{\mathrm{L}}$), are the tractions uniform along the interface and vanish in the absence of externally applied loads ($\overline{\delta} = \delta_{\mathrm{o}}$). For *non-conforming* surfaces, non-uniform interface separations and tractions arise, i.e. $\delta = \delta(x, z)$ and $T(x, z)$, and the overall average traction is:

$$\overline{T} = \frac{1}{A}\int_A T(x, z)\ \mathrm{d}x\,\mathrm{d}z = \frac{1}{A}\int_A T[\delta(x, z)]\ \mathrm{d}x\,\mathrm{d}z = \frac{1}{A}\int_A T\left[y^{\mathrm{U}}(x, z) + y^{\mathrm{L}}(x, z) + \overline{\delta}\right]\ \mathrm{d}x\,\mathrm{d}z \tag{3}$$

where A is the area of the $x - z$ plane lying in the interface.

The equilibrium separation $\delta(\overline{v} = 0) = \delta_{\mathrm{eq}}(x, z)$ satisfies:

$$\overline{T} = 0 = \frac{1}{A}\int_A T\left[\delta_{\mathrm{eq}}(x, z)\right]\ \mathrm{d}x\,\mathrm{d}z \tag{4}$$

where

$$\delta_{\mathrm{eq}}(x, z) = y^{\mathrm{U}}_{\mathrm{eq}}(x, z) + y^{\mathrm{L}}_{\mathrm{eq}}(x, z) + \overline{\delta}_{\mathrm{eq}} \tag{5}$$

Even in the absence of externally applied loads, the upper and lower interface surfaces undergo deformations at the equilibrium state due to the existence of non-uniform interface tractions. Those deformations, $y^{\mathrm{U}} = y^{\mathrm{U}}_{\mathrm{eq}}(x, z)$ and $y^{\mathrm{L}} = y^{\mathrm{L}}_{\mathrm{eq}}(x, z)$, as well as the separation between the bounding planes, $\overline{\delta} = \overline{\delta}_{\mathrm{eq}}$,[1] at equilibrium satisfy:

$$0 = \frac{1}{A}\int_A T\left[y^{\mathrm{U}}_{\mathrm{eq}}(x, z) + y^{\mathrm{L}}_{\mathrm{eq}}(x, z) + \overline{\delta}_{\mathrm{eq}}\right]\ \mathrm{d}x\,\mathrm{d}z \tag{6}$$

For rigid bulk behavior, where $y^{\mathrm{U}}_{\mathrm{eq}} = y^{\mathrm{U}}_{\mathrm{o}}(x, z)$ and $y^{\mathrm{L}}_{\mathrm{eq}} = y^{\mathrm{L}}_{\mathrm{o}}(x,z)$, the solution to (6) only involves the determination of $\overline{\delta}_{\mathrm{eq}}$ because for *non-conforming* surfaces $\overline{\delta}_{\mathrm{eq}} \neq \delta_{\mathrm{o}}$. In the case of deformable bulk solids, even at equilibrium the surface profiles $y^{\mathrm{U}}_{\mathrm{eq}}(x, z)$ and $y^{\mathrm{L}}_{\mathrm{eq}}(x, z)$ differ from the as-fabricated profiles $y^{\mathrm{U}}_{\mathrm{o}}(x, z)$ and $y^{\mathrm{L}}_{\mathrm{o}}(x, z)$.

Given solutions $T[y^{\mathrm{U}}(x, z) + y^{\mathrm{L}}(x, z) + \overline{\delta}]$ that correspond to an overall displacement $\overline{v}$ acting on the deformable bulk solid and the average traction from (3), one can deduce the $\overline{\delta}(\overline{v})$ relation, the load-displacement relation, $\overline{T} - \overline{v}$, and the effective interface traction-separation relation, $\overline{T} - \overline{\delta}$. The maximum average traction at the separation $\overline{\delta}_{\mathrm{eq}} + \overline{\delta}_{\mathrm{m}}$ of the bounding planes corresponds to $\mathrm{d}\overline{T}/\mathrm{d}\overline{v} = 0$ at the applied displacement $\overline{v}_{\mathrm{m}}$, which from (3) is found from the interface opening $\delta(x, z)$ that maximizes the traction with respect to $\overline{v}$:

$$max_{\overline{v}}\ \left\{\frac{1}{A}\int_A T[\delta(x, z)]\ \mathrm{d}x\,\mathrm{d}z\right\} \tag{7}$$

The solution $\overline{v} = \overline{v}_{\mathrm{eq}} + \overline{v}_{\mathrm{m}}$ to (7) also implies that $\overline{\delta}_{\mathrm{m}}$, $y^{\mathrm{U}}_{\mathrm{m}}(x, z)$, $y^{\mathrm{L}}_{\mathrm{m}}(x, z)$ and $\overline{\delta}_{\mathrm{eq}}$ determine the maximum average traction:

$$\overline{T}_{\max} = \frac{1}{A}\int_A T\left[y^{\mathrm{U}}_{\mathrm{m}}(x, z) + y^{\mathrm{L}}_{\mathrm{m}}(x, z) + \overline{\delta}_{\mathrm{eq}} + \overline{\delta}_{\mathrm{m}}\right]\ \mathrm{d}x\,\mathrm{d}z \tag{8}$$

Given the general relation $\overline{\delta}(\overline{v})$, the maximum traction can be regarded as a function of either $\overline{\delta}_{\mathrm{m}}$ or $\overline{v}_{\mathrm{m}}$. This problem is relatively simple for rigid bulk solids, since $y^{\mathrm{U}}_{\mathrm{m}} = y^{\mathrm{U}}_{\mathrm{o}}(x, z)$ and $y^{\mathrm{L}}_{\mathrm{m}} = y^{\mathrm{L}}_{\mathrm{o}}(x, z)$, therefore $\overline{v}_{\mathrm{m}} = \overline{\delta}_{\mathrm{m}}$ is the only unknown. In general, surface profiles $y^{\mathrm{U}}_{\mathrm{m}}(x, z)$ and $y^{\mathrm{L}}_{\mathrm{m}}(x, z)$ must be determined from the complete solutions for the deformable solids interacting across the patterned interface according to the TSR in (1) (as seen in Fig. 1).

For the displacement loading condition defined above, the work of separation for the patterned interface is:

$$\begin{aligned}\overline{W} &= \int_0^\infty \overline{T}(\overline{v})\ \mathrm{d}\overline{v} = \frac{1}{A}\int_0^\infty \left\{\int_A T[\delta(x, z)]\ \mathrm{d}x\,\mathrm{d}z\right\}\ \mathrm{d}\overline{v} \\ &= \frac{1}{A}\int_{\overline{\delta}_{\mathrm{eq}}}^\infty \left\{\int_A T\left[y^{\mathrm{U}}(x, z) + y^{\mathrm{L}}(x, z) + \overline{\delta}\right]\ \mathrm{d}x\,\mathrm{d}z\right\}\ \mathrm{d}\overline{\delta}\end{aligned} \tag{9}$$

The above applies to 2D patterned surfaces, while the results in the remainder of the paper consider 1D patterned surfaces that are uniform in the z– direction, which leads to 2D boundary-value problems for deformable bulk solids. The effects of patterning on the overall effective traction-separation relations are readily investigated in this 2D case.

Two important non-dimensional parameters enter the analyses in this paper. For a given intrinsic TSR, the interface geometry and pattern height h_0 (defined below for specific patterns) strongly influence the traction distributions and, therefore, the effective interfacial strength $\overline{T}_{\max}$ and the work of separation $\overline{W}$. One non-dimensional parameter is the ratio of pattern height to the intrinsic interaction range:

$$\eta = h_0/\delta_{\mathrm{m}} \tag{10}$$

---

[1] Throughout this paper, an overbar denotes an overall solution variable associated with a patterned interface, including effective properties such as $\overline{\delta}$, $\overline{\delta}_{\mathrm{eq}}$, $\overline{T}_{\max}$, $\overline{\delta}_{\mathrm{m}}$, and $\overline{W}$; field variables such as the traction distribution $T(x, z)$ for the patterned interface are not denoted with an overbar.

Recall that for the TSR in (1) with small α, $\delta_{\mathrm{m}} \approx \beta$. For a given pattern, as η increases, the effects of *non-conformity* between the adhering surfaces increases and, intuitively, $\overline{T}_{\max}$ and $\overline{W}$ tend to decrease. Another non-dimensional parameter reflects the importance of bulk deformation:

$$\lambda = \frac{\sigma_{\max}}{\delta_{\mathrm{m}}}\left(\frac{H}{E}\right)^{*} \tag{11}$$

where, for deformable upper and lower solids on either side of the interface, $(H/E)^{*} = H^{\mathrm{U}}(1-\nu^{\mathrm{U}^2})/E^{\mathrm{U}} + H^{\mathrm{L}}(1-\nu^{\mathrm{L}^2})/E^{\mathrm{L}}$, with the height, Young's modulus and Poisson's ratio of the upper and lower bulk solids, respectively, H^{U}, E^{U}, and ν^{U} and H^{L}, E^{L}, and ν^{L}.

Rigid bulk behavior corresponding to $\lambda = 0$ is considered in the next section for a variety of patterned surfaces. In Section 5, finite element calculations are carried out for a periodically patterned surface with the bulk solids undergoing small strain deformations and isotropic, linear elastic behavior ($\lambda \neq 0$). These solutions determine the interface profiles and the separations that enter into (2), which then determine the interface traction distributions from (1), the effective TSR from (3), and the effective properties given in (6) – (9).

4. Adhesion of patterned surfaces – rigid bulk behavior

Non-uniform tractions generally exist across the interface between *non-conforming* surfaces, even at equilibrium in the absence of external loading (see Fig. 2 as an example) and vary continuously as the surfaces are being separated. Whether the bulk solids are rigid or deformable, the traction distribution depends on the overall applied load. To study the role of geometry, adhesion of five periodically patterned surfaces to a flat substrate is investigated in this section under the assumption that both solids are rigid (non-deforming). The patterns are 1D, varying only with x, i.e. independent of z, in which case $y^{\mathrm{U}} = y_{\mathrm{o}}^{\mathrm{U}}(x)$ and $y^{\mathrm{L}} = y_{\mathrm{o}}^{\mathrm{L}}(x)$. Closed form solutions are readily obtained and evaluated numerically. The five geometries depicted in Fig. 3 are characterized by a pattern height h_0 and wavelength L and include: cosine $\{h(x) = (h_0/2)[1 + \cos(2\pi x/L)]\}$, flattened cosine $\left\{h(x) = (h_0/2)\left(1 + \sin\left[\frac{1}{2}\pi\cos(2\pi x/L)\right]\right)\right\}$, saw tooth (isosceles triangle), rectangle (equal upper and lower flat segment length), and isosceles trapezoid (equal spans of upper, lower, and diagonal segments). For rigid bulk behavior, the separation between the top and bottom surfaces of the bulk solids is expressed as:

$$\delta(x) = h(x) + \overline{\delta} \tag{12}$$

where $h(x) = y_{\mathrm{o}}^{\mathrm{U}}(x)$ defines the surface topography of the upper bulk solids.

4.1. Effective adhesion properties

The traction varies along the patterned interface as a function of the local separation $\delta(x)$. With $y^{\mathrm{L}} = 0$ as the surface of the bottom substrate, the local traction $T[h(x) + \overline{\delta}]$ varies with x, and the average traction $\overline{T}$ for a period of length L is:

$$\overline{T}(h_0, \overline{\delta}) = \frac{1}{L}\int_0^L T[h(x) + \overline{\delta}]dx \tag{13}$$

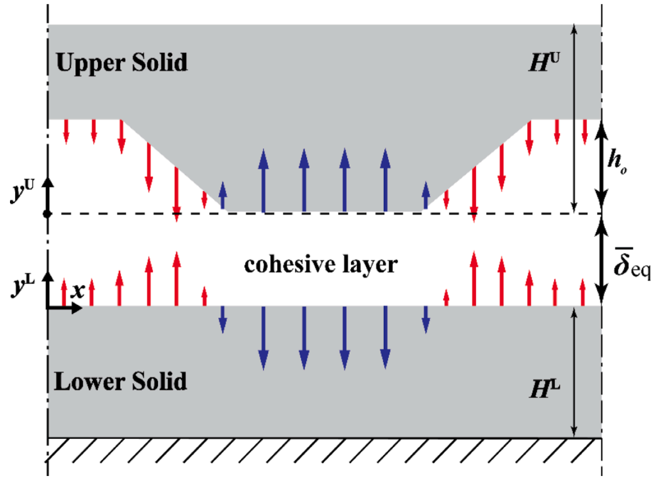

Fig. 2. An isosceles trapezoidal-patterned *non-conformal* interface at equilibrium configuration in which both attractive (red arrows) and repulsive (blue arrows) tractions exist. For rigid bulk in the absence of external loading, the tractions are a function of the local separation $\delta_{\mathrm{eq}}(x) = h(x) + \overline{\delta}_{\mathrm{eq}}$.

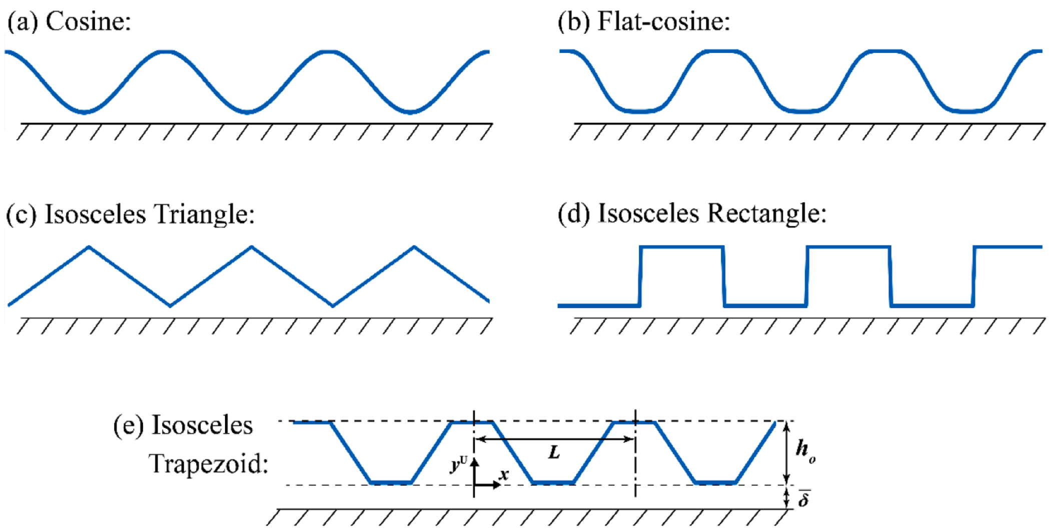

Fig. 3. Five periodic surface geometries are depicted in unstressed configuration, including (a) cosine, (b) flattened cosine, (c) isosceles triangle, (d) isosceles rectangle, and (e) isosceles trapezoid. Each geometry is characterized by a pattern height h_0 and wavelength L. Note that the height of each pattern is magnified in these images, while generally the configurations with controllable adhesion correspond to $h_0/L << 1$.

and this specifies the overall effective traction-separation relation, $\overline{T} - \overline{\delta}$. At equilibrium when $\overline{T} = 0$, the traction distribution $T[\delta(x)]$ is non-zero wherever $\delta_{\mathrm{eq}}(x) = h(x) + \overline{\delta}_{\mathrm{eq}} \neq \delta_{\mathrm{o}}$ for *non-conforming* surfaces. The effective equilibrium separation $\overline{\delta}_{\mathrm{eq}}$, here defined as the gap between the flat substrate and the lowest point of the patterned surface (see Fig. 2), is found as the root of:

$$\overline{T}\left(h_0, \overline{\delta}_{\mathrm{eq}}\right) = 0 \tag{14}$$

The maximum overall average traction $\overline{T}_{\max}$ at separation $\overline{\delta}_{\mathrm{eq}} + \overline{\delta}_{\mathrm{m}}$, from (13), is

$$\overline{T}_{\max} = \overline{T}\left(h_0, \overline{\delta}_{\mathrm{eq}} + \overline{\delta}_{\mathrm{m}}\right) \tag{15}$$

where $\overline{\delta}_{\mathrm{m}}$, the effective range of interactions for the patterned interface, is the root of:

$$\frac{d\overline{T}}{d\overline{\delta}} = 0 = \frac{1}{L}\int_0^L \frac{dT\left[h(x) + \overline{\delta}_{\mathrm{eq}} + \overline{\delta}_{\mathrm{m}}\right]}{d\overline{\delta}}\, dx \tag{16}$$

Finally, the work of separation (9) becomes:

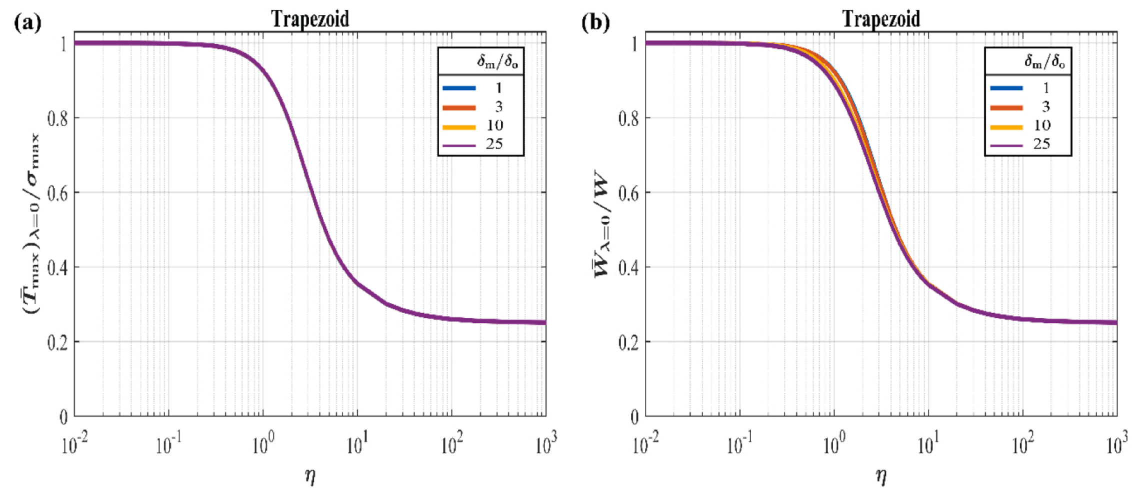

Fig. 4. Normalized (a) effective adhesive strength $(\overline{T}_{\max})_{\lambda=0}$ and (b) the work of separation $\overline{W}_{\lambda=0}$ as function of $\eta = h_{\mathrm{o}}/\delta_{\mathrm{m}}$ for the periodic trapezoidal-patterned interface.

$$\overline{W} = \int_0^\infty \overline{T}(\overline{v})\,\mathrm{d}\overline{v} = \frac{1}{L}\int_0^\infty \left\{ \int_0^L T[h(x)+\delta(x)]\mathrm{d}x \right\} \mathrm{d}\overline{v} \tag{17}$$

4.2. *Isosceles trapezoidal pattern*

Consider the isosceles trapezoidal pattern of Fig. 3e first, which consists of $1/4L$ upper flat segment, $1/4L$ lower flat segment, and two diagonal surfaces that span $1/4L$ each. For the TSR in (1) with input properties ψ, δ_o, α, and β (or the associated intrinsic properties W, δ_o, δ_m and σ_max), both $(\overline{T}_\mathrm{max})_{\lambda=0}$ and $\overline{W}_{\lambda=0}$ (normalized by the corresponding values for an ideally flat interface) decrease as the normalized pattern height ratio η increases as seen in Fig. 4. Furthermore, both $(\overline{T}_\mathrm{max})_{\lambda=0}$ and $\overline{W}_{\lambda=0}$ display asymptotes for small and large η. From dimensional analysis, in addition to the η dependence, there can also be dependencies on $\delta_\mathrm{m}/\delta_\mathrm{o}$ (or β/δ_o) and α. For small α, both of those dependencies are found to be very small and, therefore, we regard these trends in the rigid bulk case for a given type of pattern as “master curves” that are characteristic of the type of pattern in the rigid bulk limit. Results for much larger values of $\delta_\mathrm{m}/\delta_\mathrm{o}$ (not shown here) also approximate the same master curve as function of η.

The master curves can be divided into three regimes, which can serve as a guidance for adhesion control via surface patterning for a given geometry (see Fig. 4): i) the relatively smooth regime corresponding to small η in which case $(\overline{T}_\mathrm{max})_{\lambda=0}$ and $\overline{W}_{\lambda=0}$ asymptote to their ideally-flat interface values, ii) the geometry-sensitive regime for intermediate η, and iii) the large η asymptote. In the case of the trapezoidal pattern, the limits of $(\overline{T}_\mathrm{max})_{\lambda=0}$ and $\overline{W}_{\lambda=0}$ for large η are non-zero and correspond to the dominant interactions along the lower flat segment of the trapezoidal pattern, which spans $1/4L$. Intrinsic adhesion properties are recovered in the smooth regime, $0 < \eta \lesssim 10^{-1}$, where both $(\overline{T}_\mathrm{max})_{\lambda=0}$ and $\overline{W}_{\lambda=0}$ are insensitive to interface pattern height. The geometry-sensitive regime ranges $10^{-1} \lesssim \eta \lesssim 10^{2}$ and corresponds to a monotonic decrease in both $(\overline{T}_\mathrm{max})_{\lambda=0}$ and $\overline{W}_{\lambda=0}$. For $\eta \gtrsim 10^{2}$, both $(\overline{T}_\mathrm{max})_{\lambda=0}$ and $\overline{W}_{\lambda=0}$ approach their asymptotic limits (insensitive to interface pattern height again), which for the isosceles trapezoidal pattern are one-fourth of the values for an ideally-flat interface, e.g. $1/4(\overline{T}_\mathrm{max})_{\lambda=0}$.

Distinguishing the traction distributions across the different segments of the interface pattern can help us understand the various behaviors of the effective properties. Fig. 5 partitions the total traction contribution of $(\overline{T}_\mathrm{max})_{\lambda=0}$ in Fig. 4a into the upper flat segment, the diagonals, and the lower flat segment of the trapezoidal pattern. Note that both the upper and lower flat segments span $1/4L$ each, and the two diagonal surfaces together span $1/2L$. In the smooth regime of smaller η, each segment of the pattern contributes equally to the total $(\overline{T}_\mathrm{max})_{\lambda=0}$, meaning that traction distribution across the interface is essentially uniform. In the geometry-sensitive regime, the contribution of each segment varies as η increases. The contribution of upper flat segment of the pattern is the first to decrease to zero as it is far beyond the interaction range of intrinsic TSR as pattern height ratio increases, which essentially reduces the effective adhesion area. As η increases further, the diagonal surfaces move beyond the interaction range and their contributions also tend to vanish, leaving only the lower flat segment of the pattern to contribute to the asymptotic value $(\overline{T}_\mathrm{max})_{\lambda=0}$. Not that the contribution from the lower flat segment has a minimum around $\eta = 2$ as the results are nearly geometry sensitive but depend weakly on $\delta_\mathrm{m}/\delta_\mathrm{o}$ (or β/δ_o) and α.

The variations of the effective length scales $(\overline{\delta}_\mathrm{eq})_{\lambda=0}$ and $(\overline{\delta}_\mathrm{m})_{\lambda=0}$ as function of η for the trapezoidal pattern are plotted in Fig. 6 for

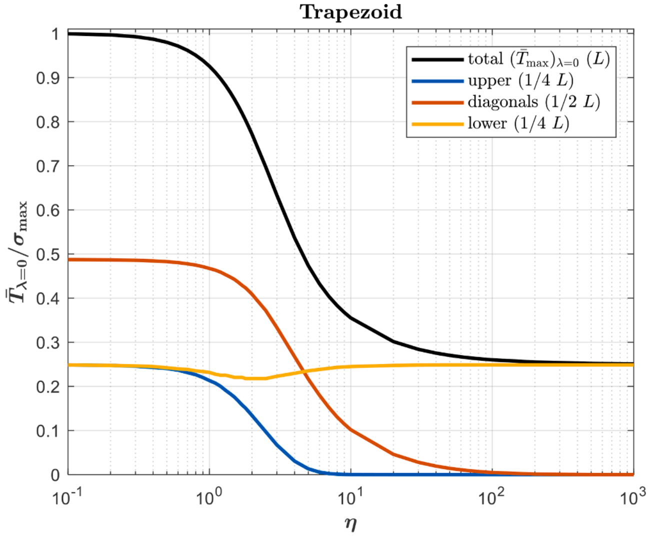

Fig. 5. At $(\overline{T}_\mathrm{max})_{\lambda=0}$, contributions to (15) from different segments of the trapezoidal pattern vs η for $\delta_\mathrm{m}/\delta_\mathrm{o} = 3$ and $\alpha = 0.01$. The black curve is the result shown in Fig.4a. The blue curve represents the upper flat segment of the trapezoidal pattern and has length of $1/4L$. The red curve represents the two diagonal segments and has total length of $1/2L$. The yellow curve represents the lower flat segment and has length of $1/4L$.

various values of δ_m/δ_o. The strong dependence of both $(\overline{\delta}_{eq})_{\lambda=0}$ and $(\overline{\delta}_m)_{\lambda=0}$ on δ_m/δ_o can be understood as follows. For a very small pattern height ratio η, both $(\overline{\delta}_{eq})_{\lambda=0}$ and $(\overline{\delta}_m)_{\lambda=0}$ approach their intrinsic values because tractions across the interface are relatively uniform. As η increases, interface tractions become more non-uniform, and to achieve equilibirum the lower segment of the patterned surface approaches the substrate, leading to repulsive tractions. For larger η, the dominant interactions essentially are confined to the lower flat segment of the trapezoidal pattern (see Fig. 5) and the interface tractions become more uniform, with both $(\overline{\delta}_{eq})_{\lambda=0}$ and $(\overline{\delta}_m)_{\lambda=0}$ approaching their corresponding intrinsic values once again. Therefore, $(\overline{\delta}_{eq})_{\lambda=0}$ and $(\overline{\delta}_m)_{\lambda=0}$ vary non-monotonically with η and depend on the ratio of the intrinsic length scales, δ_m/δ_o. For the isoscoles trapezoidal pattern, the minima of $(\overline{\delta}_{eq})_{\lambda=0}$ and $(\overline{\delta}_m)_{\lambda=0}$ correspond approximately to $\eta = 2$ (Fig. 6), which is in the geometry sensitive regime of the master curves.

4.3. Variations in pattern designs

The other four patterns depicted in Fig. 3 are considered next for rigid bulk behavior. For each pattern, the $(\overline{T}_{max})_{\lambda=0}$ and $\overline{W}_{\lambda=0}$ variations with respect to $\eta = h_0/\delta_m$ are found to depend weakly on δ_m/δ_o as in the case of the trapezoidal pattern considered in Sec. 4.2. Fig. 7 are plots of the master curves corresponding to $\delta_m/\delta_o = 3$ and $\alpha = 0.01$. Similar trends are found for all five patterns for small and moderate values of η, and 3 regimes are identified: i) the smooth regime of small η, ii) the geometry-sensitive regime for intermediate η, and iii) the large η asymptote. As η increases beyond the relatively smooth regime, there is a portion in the geometry-sensitive regime where the $(\overline{T}_{max})_{\lambda=0}$ and $\overline{W}_{\lambda=0}$ trends are similar for the 5 patterns, see Fig. 7a, b, that is approximately the range $10^{-1} \lesssim \eta \lesssim 4$ in which $(\overline{T}_{max})_{\lambda=0}$ and $\overline{W}_{\lambda=0}$ are relatively insensitive to the specific pattern shape. However, for $\eta \gtrsim 4$, there are significant differences among the 5 patterns. For very large η, the trapezoidal pattern asymptotes to $1/4L$ (as noted above), and the rectangular pattern asymptotes to $1/2L$; both determined by simple geometric considerations. The other three patterns asymptote to zero values of $(\overline{T}_{max})_{\lambda=0}$ and $\overline{W}_{\lambda=0}$ as $\eta \to \infty$.

Interestingly, the triangular and rectangular patterns bound the $(\overline{T}_{max})_{\lambda=0}$ and $\overline{W}_{\lambda=0}$ variations with respect to η among the five isosceles shapes (Fig. 7a, b). For $\eta \lesssim 4$, the triangular pattern has the highest values and the rectangular pattern has the lowest values of $(\overline{T}_{max})_{\lambda=0}$ and $\overline{W}_{\lambda=0}$; for $\eta \gtrsim 4$, the rectangular pattern has the highest values and the triangular pattern has the lowest values of $(\overline{T}_{max})_{\lambda=0}$ and $\overline{W}_{\lambda=0}$. The switch in adhesion performance can be understood as follows. For $\eta \lesssim 4$, diagonal surfaces of the triangular pattern create non-uniform interface gaps that span the full range of the intrinsic TSR, thus, leading to non-uniform interface tractions. On the other hand, the flat segments of the rectangular pattern have uniform gap size and interface tractions across each segment, and these tractions either uniformly increase from $\overline{T}(\overline{\delta}_{eq}) = 0$ or uniformly decay as the separation increases. Furthermore, for $\eta \gtrsim 4$, the effective adhesion area of a diagonal surface gradually shrinks as the interface is separated, while the adhesion area of the flat portion of the surface remains unchanged (see Fig. 5).

For all *non-conforming* patterns, the variations of the effective equilibrium separation $(\overline{\delta}_{eq})_{\lambda=0}$ and the effective interaction range $(\overline{\delta}_m)_{\lambda=0}$ with respect to η generally depend on δ_m/δ_o, as in the case of the trapezoidal pattern (see Fig. 6). As a representative case, variations with respect to η for the five patterns are plotted in Fig. 7c, d for $\delta_m/\delta_o = 3$.

For a given pattern, the rigid bulk results can be understood in more detail by examining the interface traction distributions $T(x,\overline{\delta})$, which in fact have been calculated to generate the results above; see (13) and (17). In fact, those distributions vary significantly as $\overline{\delta}$

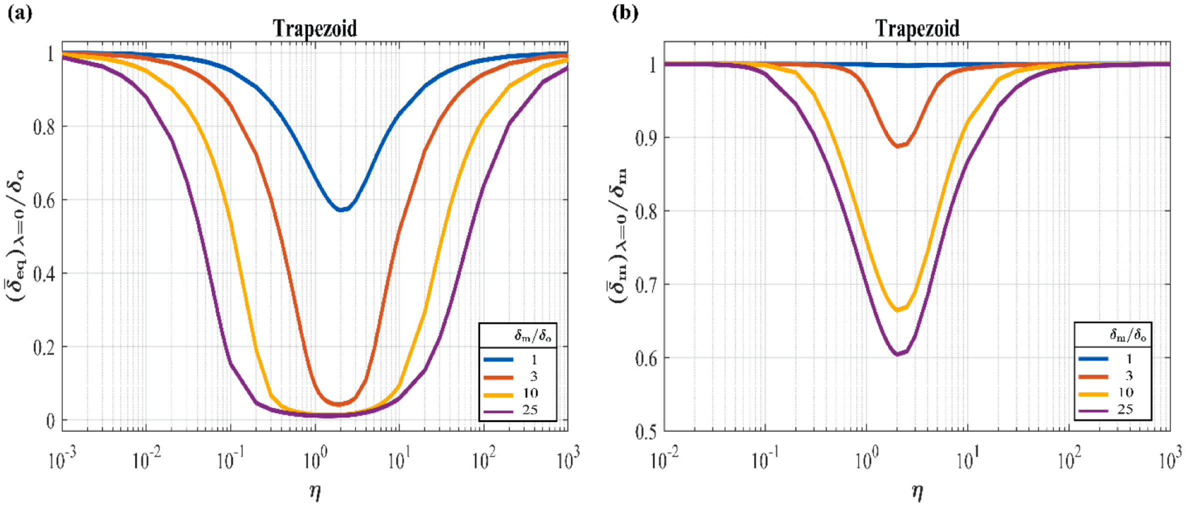

Fig. 6. Normalized (a) effective equilibrium separation $(\overline{\delta}_{eq})_{\lambda=0}$, and (b) effective interaction range $(\overline{\delta}_m)_{\lambda=0}$ as function of η for the periodic trapezoidal-patterned interface.

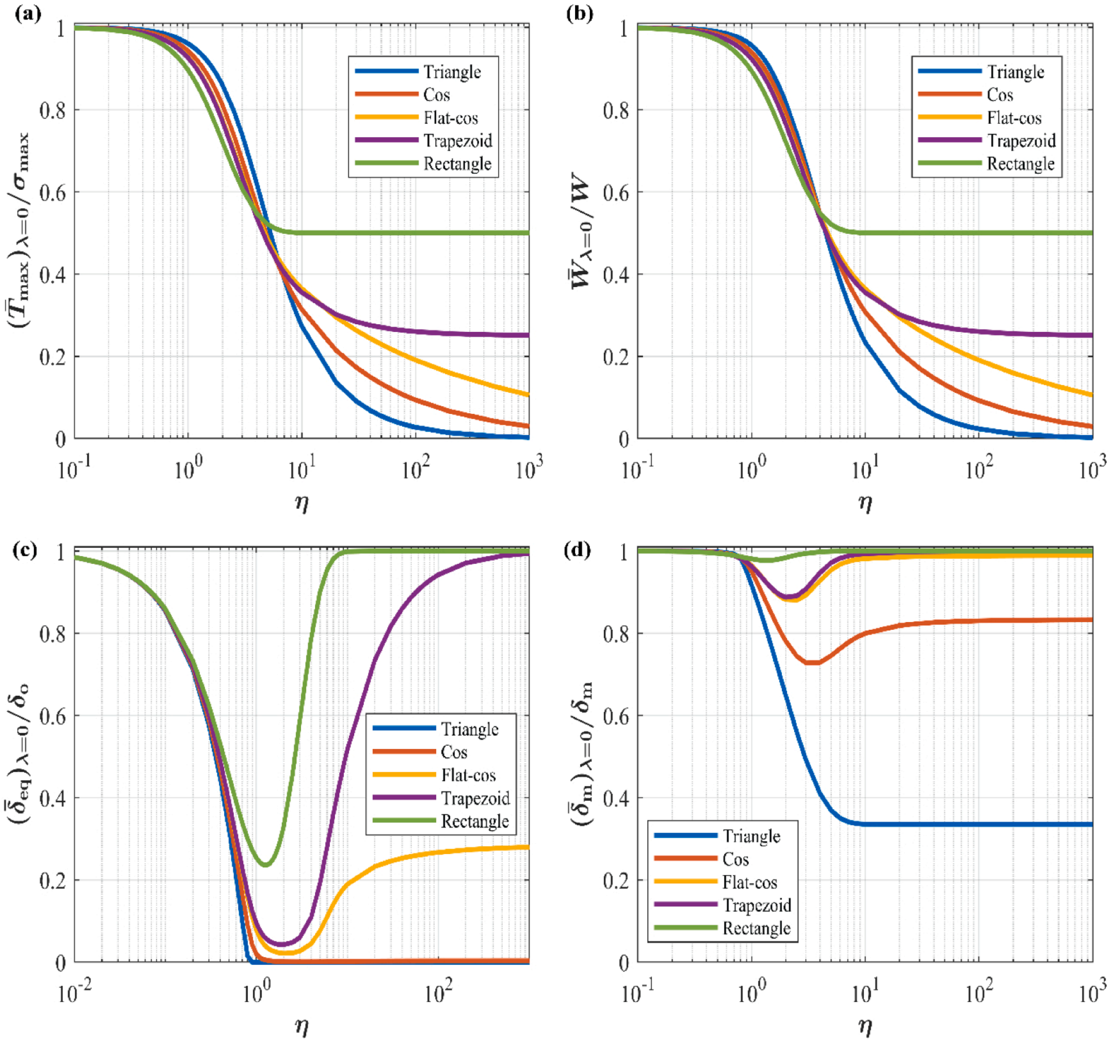

Fig. 7. Effective adhesive properties of rigid bulk behavior with $\delta_m/\delta_o = 3$ and $\alpha = 0.01$ for all five geometries. Master curves showing normalized (a) effective adhesive strength $(\overline{T}_{max})_{\lambda=0}$ and (b) work of separation $\overline{W}_{\lambda=0}$. Normalized (c) effective equilibrium separation $(\overline{\delta}_{eq})_{\lambda=0}$ and (d) effective interaction range $(\overline{\delta}_m)_{\lambda=0}$.

increases from $(\overline{\delta}_{eq})_{\lambda=0}$ to $(\overline{\delta}_m)_{\lambda=0}$ and beyond. For example, on segments of the interface topography where $\delta(x) = h(x) + \overline{\delta} >> \delta_m$, the local traction $T(x, \overline{\delta})$ becomes arbitrarily small, which accounts for the large η trends in $(\overline{T}_{max})_{\lambda=0}$ and $\overline{W}_{\lambda=0}$. For brevity, those traction distributions $T(x, \overline{\delta})$ across the interface as function of $\overline{\delta}$ have not been plotted for the rigid bulk behaviors, while the distributions calculated from the finite element solutions presented in the next section reveal those variations.

5. Adhesion of patterned surfaces – effects of elastic bulk deforamtion

Elastic bulk deformation ($\lambda \neq 0$) can significantly affect adhesion of *non-conformal* patterned interfaces by altering the surface topography, while for sufficiently stiff materials the rigid analysis ($\lambda = 0$) is an accurate approximation. For soft bulk, the surface topography at equilibrium, which involves non-zero and non-uniform surface tractions for *non-conforming* interfaces, will be distorted as compared to its as-fabricated geometry in the absence of surface tractions, i.e.$y^{U}_{eq} \neq y^{U}_{o}(x)$ for $\lambda \neq 0$. Finite element solutions presented in this section are for a *non-conforming* interface with isosceles trapezoidal pattern and varied elastic bulk properties as function of the bulk deformation parameter λ (11) and the pattern height parameter η (10). As a general trend, in the absence of any applied load, i.e. at equilibrium, the interface profile tends to become flatter, which is analogous to the increase in contact area found in the work of Johnson et al. (1985).

One general effect of elastic bulk deformation, even for flat interfaces, is the tendency for spring-back. Spring-back occurs as the overall load decreases after reaching its maximum, which is associated with the decrease in the average adhesive traction across the interface as separation increases, thus causing a decrease in the elastic strain in the bulk solids to decrease. The decreasing elastic strain contributes to the decrease in the overall extension of the bulk solids as the interface continues to separate and is directly related to the bulk stiffness and the heights of the bulk solids adjacent to the interface. Consider a rectangular block of linear elastic, isotropic material with tensile modulus E^{U} and height H^{U}, where the lower surface of this block interacts with a rigid flat substrate, $E^{\mathrm{L}} \rightarrow \infty$, according to the TSR in (1). From the equilibrium configuration, the top of the block is displaced by $\bar{v}$ perpendicular to the interface. The block is assumed to be under a state of plane-strain, and the corresponding applied traction is denoted $\overline{T}$. If the block is relatively soft and/or tall and as the interface is separated beyond the maximum traction $\sigma_{\max}$ (or the maximum load $\overline{T}_{\max}$ in (8) or (15) for a patterned interface), spring-back can occur due to unloading of the elastic block as discussed below.

The non-dimensional deformation ratio, λ (11), that reflects the tendency for the surface pattern to be distorted and the tendency for spring back, in this case of a rigid substrate is:

$$\lambda = \frac{\sigma_{\max}}{\delta_{\mathrm{m}}}\left[\frac{H^{\mathrm{U}}\left(1-\nu^{\mathrm{U}^2}\right)}{E^{\mathrm{U}}}\right] \tag{18}$$

For large enough λ, very little overall extension beyond maximum load is possible, as shown in Fig. 8. While spring-back can be captured in numerical simulations (e.g., using continuation algorithms), it would be difficult to detect in experiments under either displacement- or force-controlled test. In an experiment, attempts to further increase the overall extension beyond the maximum load would lead to sudden failure where the force would drop down to zero instantaneously, and the resulting load-and-displacement curve could lead to apparently longer interaction range and the interface toughness would not be properly accounted for.

The master curves in Fig. 7a, b have shown that all five geometries display similar trends for the key effective properties. In what follows, the isosceles trapezoidal pattern is chosen as the representative for the investigation of the effects of elastic bulk deformation because it includes the rectangular and triangular patterns as special cases, and, in principle, it is ameneable to fabrication. A periodic boundary-value problem is formulated. A trapezoidal-patterned unit cell is considered, as depicted in Fig. 2, consisting of a patterned top bulk solid of height H^{U} with Young's modulus E^{U} and Poisson's ratio ν^{U}, a flat rigid substrate, and a cohesive layer governed by the TSR (1) is sandwiched in between. Although the interface separation can become arbitrarily large, the bulk solid is linear elastic within the small strain approximation. The asymmetry considered here involves both the *non-conformity* of the interface topography and the moduli mismatch of the adhered solids. For the finite element results that follow, the modulus of the upper bulk solid (the one with the trapezoidal pattern) is varied, and the lower bulk solid with a flat surface is effectively rigid. Periodic boundary conditions are prescribed on the unit cell such that $u_x(0,y) = u_x(L,y)$ and $u_y(0,y) = u_y(L,y)$. The bottom of the nearly rigid substrate ($E^{\mathrm{L}} \gg E^{\mathrm{U}}$) is fixed: $u_x = u_y = 0$. From an equilibrium configuration ($\overline{T} = 0$) – which itself must be calculated since the non-zero interface tractions $T(x)$ cause bulk deformation that affects $\delta(x)$ – the top surface of the elastic bulk is displaced by an amount $u_y = \bar{v}$ with $u_x = 0$. The bulk height of the unit cell is chosen to be $H^{\mathrm{U}} = L$, and for larger H^{U} we found little change in the surface deformation for the TSR properties and range of moduli considered.

5.1. Finite element model

The unit cell problem with cohesive elements spanning the *non-conformally* patterned interface, as depicted in Fig. 2, is discretized within the commercial finite element program ABAQUS/Standard. Both bulk solids are meshed with 2D plane-strain, isotropic, linearly elastic elements. The modulus of the bottom flat solid is set high such that is effectively rigid (e.g. $E^{\mathrm{L}}/E^{\mathrm{U}} \geq 10^5$). The interface

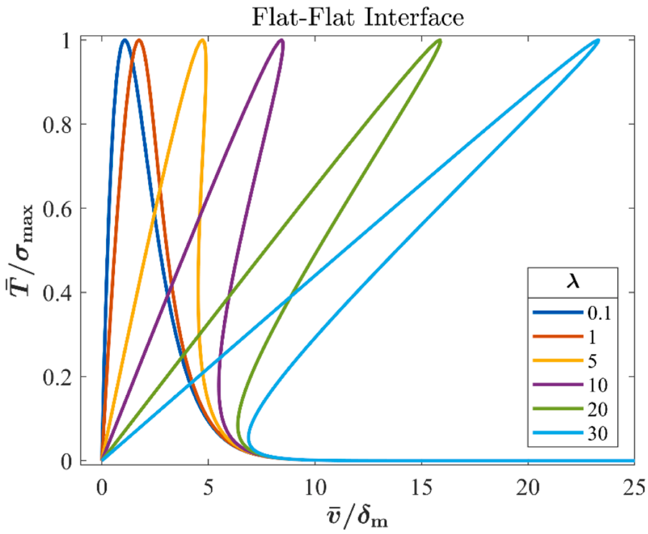

Fig. 8. For ideally flat surfaces, the effective TSR behavior for various λ with $\delta_{\mathrm{m}} = 3\delta_{\mathrm{o}}$. The tendency for spring-back increases with increasingλ.

cohesive elements are generated from a user-defined subroutine (UMAT) based upon the TSR in (1) (see the Appendix B for details of the finite element implementation). As previously noted, the surface-force mediated direct adhesion, e.g. van der Waals forces, considered in this work can arise if the normal separation between surfaces of the bulk solids is approximately in the 1∼100 nm range, with the work of adhesion in the range of $10^{-3} \sim 10^{0}$ J /m^2 (Tabor and Winterton, 1968; Israelachvili and Tabor, 1972; Israelachvili, 1974, 2011; Gao and Yao, 2004). The intrinsic TSR parameters are chosen to be: $\delta_{\rm o} = 1$ nm, $\beta = 3\delta_{\rm o}$, $\psi/\beta e = 2 \times 10^5$ Pa, where $\ln(e) = 1$, and $\alpha = 0.01$. Note from (1), the separation can be regarded in units of $\delta_{\rm o}$. The computed intrinsic properties are $\delta_{\rm m}/\delta_{\rm o} = 2.994$, $\sigma_{\max} = 2.005 \times 10^5$Pa and $W = 1.631 \times 10^{-3}$ J /m^2. Results are presented below for variations in the trapezoidal pattern height ratio (η) and in the ratio of interface to bulk deformation (λ), in particular for $10^{-4} \le \sigma_{\max}/E^{\rm U} \le 10^{-2}$, in which case $\lambda = 0.030$ to 3.039, with Poisson's ratio $\nu^{\rm U} = 0.3$.

In the initial configuration, the trapezoidal pattern is positioned at an arbitrary distance above the rigid substrate and normal tractions are assigned to each cohesive element based on the separation at the interface, which varies from element to element. That configuration is relaxed until $\overline{T} = 0$ corresponding to the equilibrium configuration at $\overline{\delta} = \overline{\delta}_{\rm eq}$ and $\overline{v} = 0$ by definition. Most studies involving cohesive zone elements have assumed uniform height of the cohesive layer at the equilibrium separation corresponding to a zero traction throughout the interface (Jiang et al., 2006; Zavattieri et al., 2007; Hossain et al., 2014; Hosseini et al., 2019). The assumption that the traction induced by van der Waals-type forces vanishes everywhere in the cohesive layer is not consistent with a spatially varying initial separation.

5.2. *Effective traction – separation relation*

The first set of results are for an interface pattern height ratio $\eta = h_0/\delta_{\rm m} = 3$. The overall load – displacement curves, $\overline{T} - \overline{v}$,

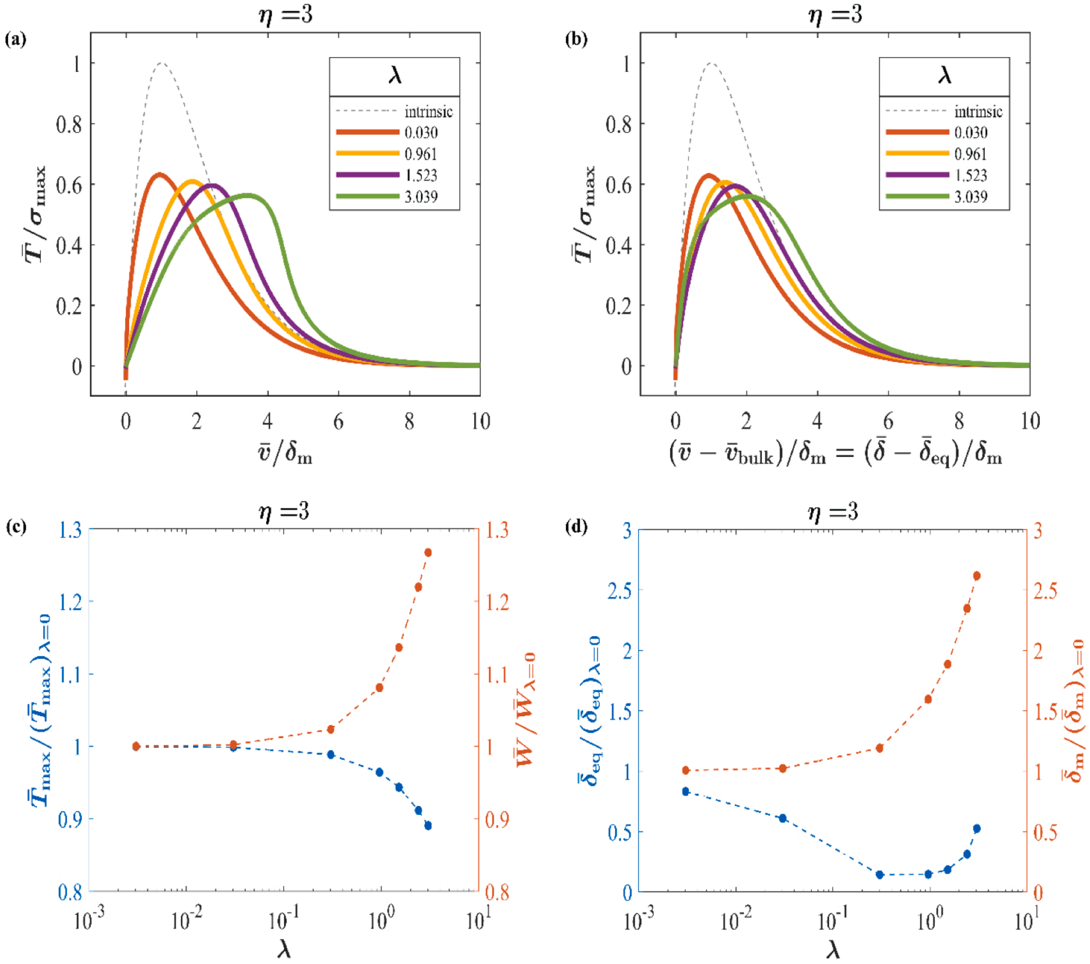

Fig. 9. Effective results for elastic bulk solid with isosceles trapezoidal surface geometry of patterned height ratio $\eta = 3$. (a) The normalized overall load – displacement curves, $\overline{T} - \overline{v}$. (b) The normalized effective TSR curve subtracts out the bulk deformation. (c) Trade-off between the effective adhesion strength and work of separation as the bulk deformation ratio λ increases. (d) Effective equilibrium separation and effective interaction range as function of λ.

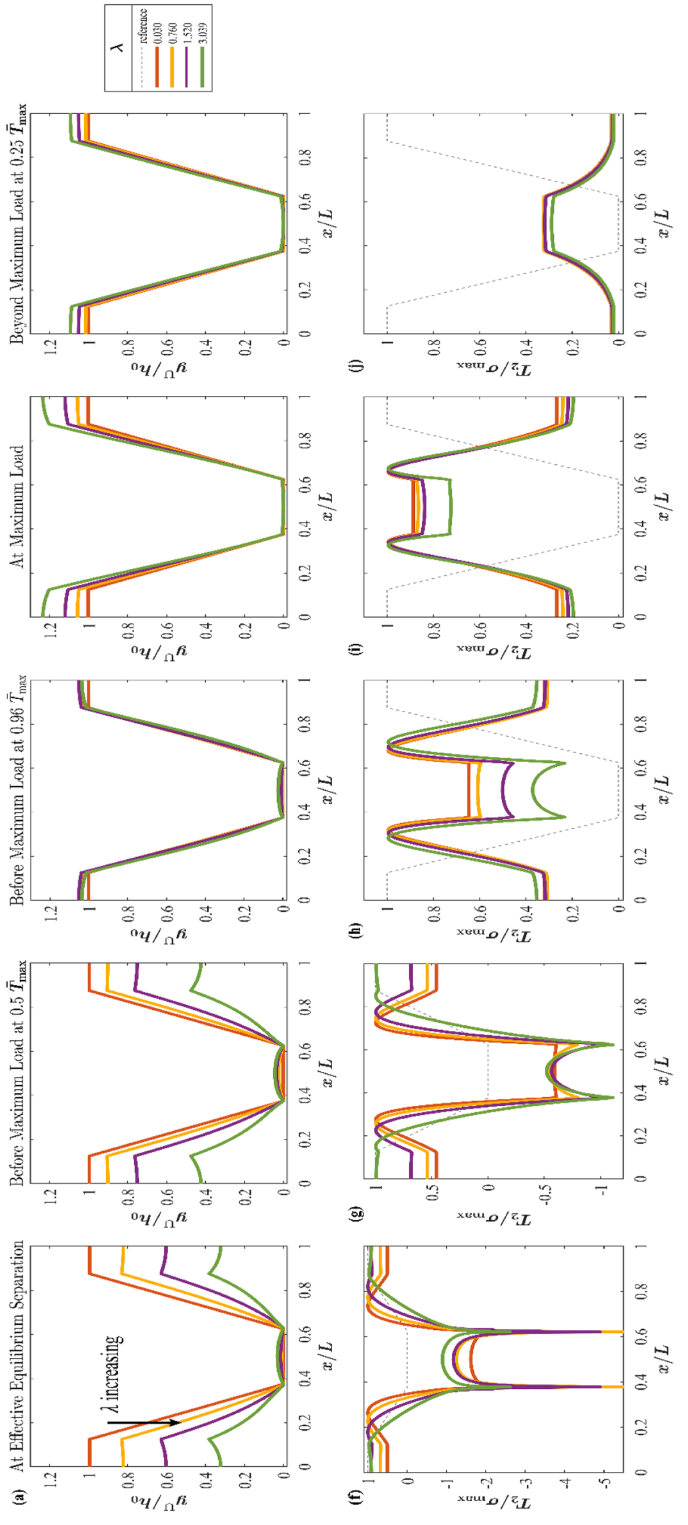

Fig. 10. Interface evolution for periodic trapezoidal pattern of $\eta = 3$. (1st row: a-e) Interface profiles and (2nd row: f-j) the corresponding interface normal traction distribution. These interfacial results are shown at (1st column: a, f) the effective equilibrium separation $\overline{\delta}_{\mathrm{eq}}$, (2nd column: b, g) before reaching maximum load $\overline{T}_{\max}$ at0.5 $\overline{T}_{\max}$, (3rd colum: c, h) before reaching maximum load $\overline{T}_{\max}$ at 0.96 $\overline{T}_{\max}$, (4th colum: d, i) at maximum load $\overline{T}_{\max}$, and (5th column: e, j) after passing maximum load $\overline{T}_{\max}$ at 0.25 $\overline{T}_{\max}$.

computed from the finite element solutions are plotted in Fig. 9a for various values of the bulk deformation ratio λ. A significant effect of elastic bulk deformation is clearly seen. An even softer and/or taller elastic bulk solid corresponding to a larger λ would cause a greater spring-back tendency, e.g. as seen in Fig. 8, leading to some numerical difficulties which are discussed in the Appendix B. Recall that the separation between the flat rigid substrate and the lowest point of the trapezoidal-patterned surface is $\overline{\delta} = \overline{\delta}_{\text{eq}} + \overline{v} - \overline{v}_{\text{bulk}}$, where the average bulk deformation is defined as $\overline{v}_{\text{bulk}} = H^{\text{U}}[(\overline{T}/E^{\text{U}})(1 - 2{\nu^{\text{U}}}^2/(1 - \nu^{\text{U}}))]$. The resulting effective TSR defined in (3), i.e. $\overline{T}$ versus $\overline{\delta} - \overline{\delta}_{\text{eq}} = \overline{v} - \overline{v}_{\text{bulk}}$, is plotted in Fig. 9b. Even with the bulk deformation subtracted out in Fig. 9b, the effective TSR depends on the bulk deformation through its effect on distorting the patterned surface. In other words, the effective TSR for a patterned interface generally depends on the adhesive properties, i.e. the intrinsic TSR, as well as the compliance of the adjoining bulk solids.

For the four non-zero values of λ in Fig. 9a, b, the maximum average traction, $\overline{T}_{\max}$, and the work of separation, $\overline{W}$, are plotted in Fig. 9c, and the effective equilibrium separation, $\overline{\delta}_{\text{eq}}$, and effective interaction range, $\overline{\delta}_{\text{m}}$, are plotted in Fig. 9d. At $\overline{T}_{\max}$, the smallest gap is $\overline{\delta} = \overline{\delta}_{\text{eq}} + \overline{\delta}_{\text{m}}$; $\overline{\delta}_{\text{m}}$ defines an effective interaction range that can be larger than δ_{m}. Several observations can be made when comparing the results with elastic bulk deformation and the rigid results of Section4. The effective adhesive strength $\overline{T}_{\max}$ decreases as λ increases, while the work of separation $\overline{W}$ increases, as seen in Fig. 9c. In Fig. 9d, $\overline{\delta}_{\text{eq}} << \delta_{\text{o}}$ indicates that tractions across the interface become highly non-uniform for some range of λ, requiring a sector of the patterned surface to come very close to the bottom substrate to achieve equilibrium in the system, i.e., to attain sufficiently large repulsive traction. Futhermore, $\overline{\delta}_{\text{m}}$ increases as λ increases as seen in Fig. 9d. For relatively soft bulk materials, there can be significant distortions of the surface pattern due to the bulk deformations arising from the non-zero traction distributions across the interface as shown in the next section.

5.3. *Interface profiles and stress distributions*

As λ increases, elastic deformation in the bulk generally becomes important. For relatively compliant bulk solids, the interface tractions lead to distortion of the patterned surfaces, therefore affecting the degree of *non-conformity* and the overall adhesive behavior as a function of the applied load, $\overline{v}$. To understand these trends, it is useful to investigate both the non-uniform bulk deformations and the normal surface tractions acting across the interface corresponding to the results in Fig. 9. These interface traction distributions are plotted in Fig. 10 for a pattern height ratio $\eta = h_0/\delta_{\text{m}} = 3$ at five stages of the overall loading: equilibrium ($\overline{T} = 0$), before the maximum load at $\overline{T} = 0.5\,\overline{T}_{\max}$, before the maximum load at $\overline{T} = 0.96\,\overline{T}_{\max}$, at the maximum load $\overline{T}_{\max}$, and beyond the maximum load at $\overline{T} = 0.25\,\overline{T}_{\max}$.

At the effective equilibrium separation $\overline{\delta}_{\text{eq}}$, the interface profile y^{U} is plotted in Fig. 10a for various values of λ with $H^{\text{U}} = L$ fixed. As λ increases, the interface pattern height is increasingly compressed at equilibrium. The distortions of the bulk patterned surface topography in Fig. 10a arise due to the surface tractions, which are plotted in Fig. 10f for the equilibrium state. Those surface tractions reflect the interface gap associated with the trapezoidal pattern; note that the lower flat segment of the trapezoidal pattern is subjected to repulsive tractions since $\overline{\delta}_{\text{eq}} < \delta_{\text{o}}$. As $\overline{v}$ increases and the interface begins to separate, the pattern becomes relatively less compressed, corresponding to a decrease in magnitude of those repulsive tractions as well as a decrease in the attractive tractions on the upper flat segment of the trapezoidal pattern seen in Fig. 10b, g at $\overline{T} = 0.5\,\overline{T}_{\max}$ (before $\overline{T}_{\max}$ is reached). Just before reaching $\overline{T}_{\max}$, as shown in Fig. 10c, h at 0.96 $\overline{T}_{\max}$, the patterns are no longer being compressed and have returned to approximately their original heights as the lower flat segment is no longer subjected to repulsive tractions, and the magnitude of the attractive traction on the upper flat segment has decreased further for smaller λ cases. At maximum load $\overline{T}_{\max}$, with the attractive tractions greatest around the lower flat segment, the trapezoidal pattern tends to stretch, as seen in the interface profile y^{U} of Fig. 10d, which shows that the pattern height increases as λ increases. At that state, there are relatively strong attractive tractions on the lower flat segment of the trapezoidal pattern and relatively weak attractive tractions on the upper flat segment of the trapezoidal pattern, as seen in Fig. 10i. Recall that $\eta = h_0/\delta_{\text{m}} = 3$ for these results, which correlates with the latter finding. Beyond $\overline{T}_{\max}$ at $\overline{T} = 0.25\,\overline{T}_{\max}$, the interface approaches the undistorted trapezoidal geometry (see Fig. 10e), and the tractions, which are attractive everywhere along the interface, become smaller in magnitude (see Fig. 10j). As the top surface of the bimaterial sample is displaced further, the tractions become even smaller in magnitude and gradually vanish, and the surface geometry returns to its original configuration. As $\overline{\delta} \to \infty$ (and $\overline{v} \to \infty$ unless there is pronounced spring-back, which can occur for very large λ – see Fig. 8), the stresses in the bulk solid are zero everywhere in the unadhered state. Numerical difficulties associated with much larger values of λ, especially for the calculation of the equilibrium configuration, are discussed in the Appendix B. For a stiffer upper bulk solid, e.g. $\lambda \leq 0.03$, there is little effect of bulk deformation and the rigid results of Section 4 are an accurate representation.

5.4. *Effective adhesion properties*

For the case $\eta = h_0/\delta_{\text{m}} = 3$, the results in Section 5.2 have shown that the effective adhesive properties depend on the elastic bulk deformation with trends that include a decreasing $\overline{T}_{\max}$ and a increasing $\overline{W}$ as λ increases. In this section, variations in the pattern height ratio (η) are considered, again for the isosceles trapezoidal pattern interface, and the results are presented relative to both the intrinsic TSR properties and the rigid results for the patterned interfaces (from Section 4). Fig. 11a, b are plots of $\overline{T}_{\max}/\sigma_{\max}$ and $\overline{W}/W$, respectively, versus the deformation parameter λ for $0.05 \leq \eta \leq 30$. The trends are: i) $\overline{T}_{\max}/\sigma_{\max}$ and $\overline{W}/W$ both decrease with increasing pattern height, which is readily understood from the rigid results of Section 4, and ii) for each η, $\overline{T}_{\max}/\sigma_{\max}$ decreases somewhat with increasing λ, while $\overline{W}/W$ increases with increasing λ. The increase in $\overline{W}$ with increasing λ is associated with the increase in elastic strain energy as bulk material gets softer (Hensel et al., 2018). The decrease in $\overline{T}_{\max}$ with increasing λ is associated with the stretching of the pattern topography as discussed in Section 5.3 (see Fig. 10d). Hensel et al. (2018) also noted the trade-off between $\overline{T}_{\max}$ and $\overline{W}$ in adhesive contacts formed between two *non-conforming* elastic solids, that the stored elastic strain energy close to the interface counteracts adhesion strength.

Comparisons to the corresponding rigid case, $\lambda = 0$, are instructive to see how $\overline{T}_{\max}$ and $\overline{W}$ are affected by bulk deformation (normalized plots in Fig. 11c, d). For the trapezoidal-patterned interface, the “elasticity-sensitive” regime is approximately $0.5 \lesssim \eta \lesssim 30$. Overall, one concludes from Fig. 11 that surface geometry is the primary effect on the overall adhesion behavior, while the effect of elastic bulk deformation can be significant for large λ, i.e. soft solids. In the elasticity-sensitive range, both $\overline{T}_{\max}$ and $\overline{W}$ change non-monotonically as the pattern height ratio η increases. Note that the pattern height resulting in the minimum $\overline{T}_{\max}$ and maximum $\overline{W}$ is for $\eta = 3$ (the case considered in Secs. 5.2 and 5.3, which is in the geometry-sensitive regime): for $\lambda = 3.039$, compared to the rigid results, there is a 12% decrease in $\overline{T}_{\max}$ and a 28% increase in $\overline{W}$. Outside of the elasticity-sensitive regime, both $\overline{T}_{\max}$ and $\overline{W}$ are very close to the rigid results and independent of η, since the interface traction distribution is relatively uniform for very small and very large η (as explained in Secs. 4.2). Therefore, for bulk elastic solids with surface pattern heights outside of the elasticity-sensitive regime can be assumed as rigid to predict the effective interfacial adhesion properties, thus, simplifying engineering design.

For completeness, the effect of elastic bulk deformation on the effective equilibrium separation, $\overline{\delta}_{\text{eq}}$, and the effective interaction range, $\overline{\delta}_{\text{m}}$, are plotted in Fig. 12, also relative to the intrinsic properties (Fig. 12a, b) and the rigid results (Fig. 12c, d). As the elastic bulk deformation increases, $\overline{\delta}_{\text{eq}}$ tends to increase for small pattern heights (e.g., $1 \le \eta$) due to compression of the pattern but decreases for larger η (e.g., $\eta \ge 5$) when compared to the intrinsic equilibrium separation, δ_{o}. The greatest compression of surface geometry occurs for $\eta = 1$ for $\lambda \ge 3.039$ because the top flat segment of the trapezoidal pattern is subjected to the strongest attractive tractions, $T = \sigma_{\max}$, in which case $\overline{\delta}_{\text{eq}}$ is significantly larger than the rigid result, $(\overline{\delta}_{\text{eq}})_{\lambda=0}$ (Fig. 12c). Note, while $\overline{\delta}_{\text{eq}}$ is much larger than $(\overline{\delta}_{\text{eq}})_{\lambda=0}$ for $\eta = 1$, both values are still relatively small compared to the intrinsic equilibirum separation, δ_{o}. For taller patterns heights (e.g., $\eta \ge 5$), the

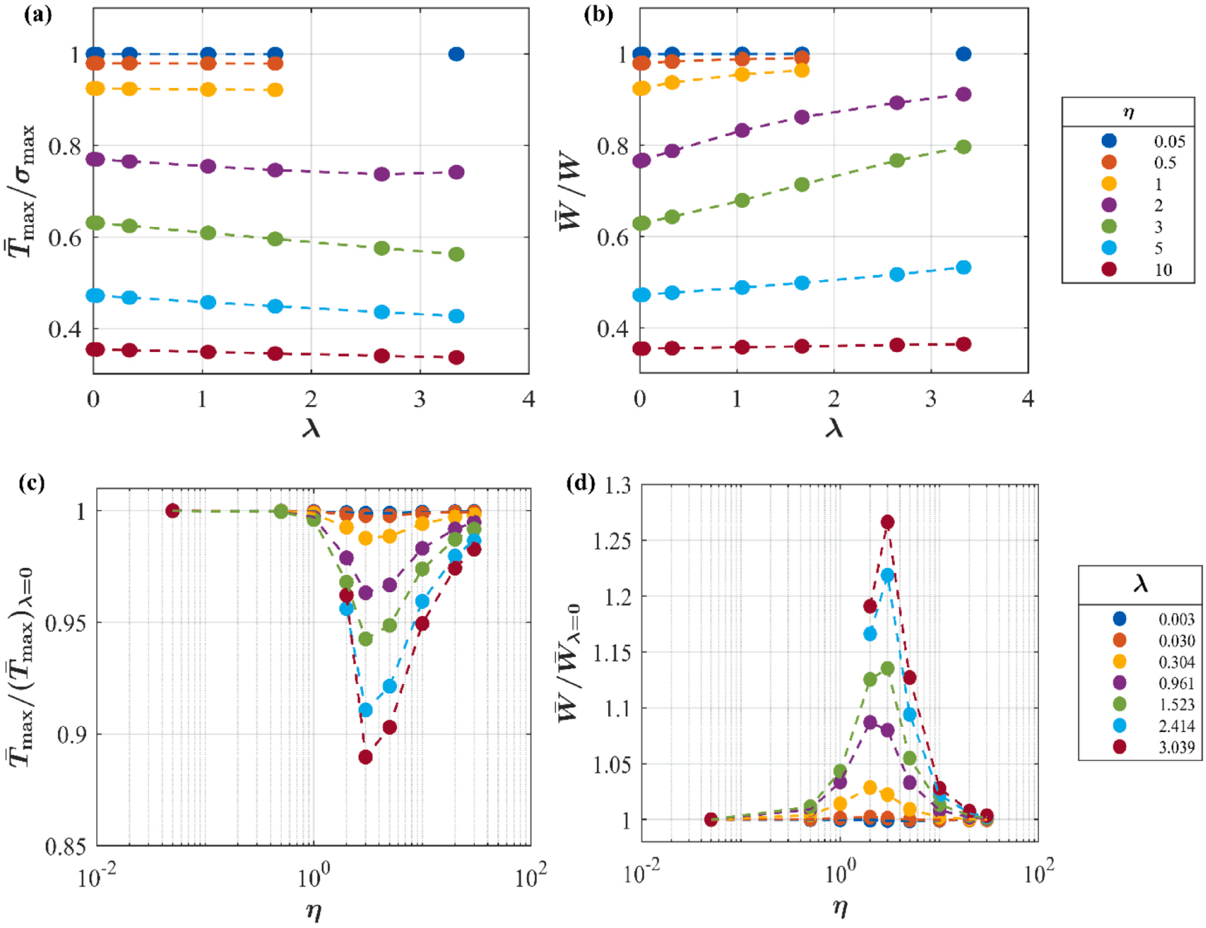

Fig. 11. Effect of elastic bulk deformation on isosceles trapezoidal pattern interface. Compared to intrinsic properties: (a) Effective adhesive strength $\overline{T}_{\max}$ and (b) work of separation $\overline{W}$ as function of deformation ratio λ for varies pattern height ratios η. Compared to rigid results: (c) $\overline{T}_{\max}$and (d) $\overline{W}$as function of η for various λ.

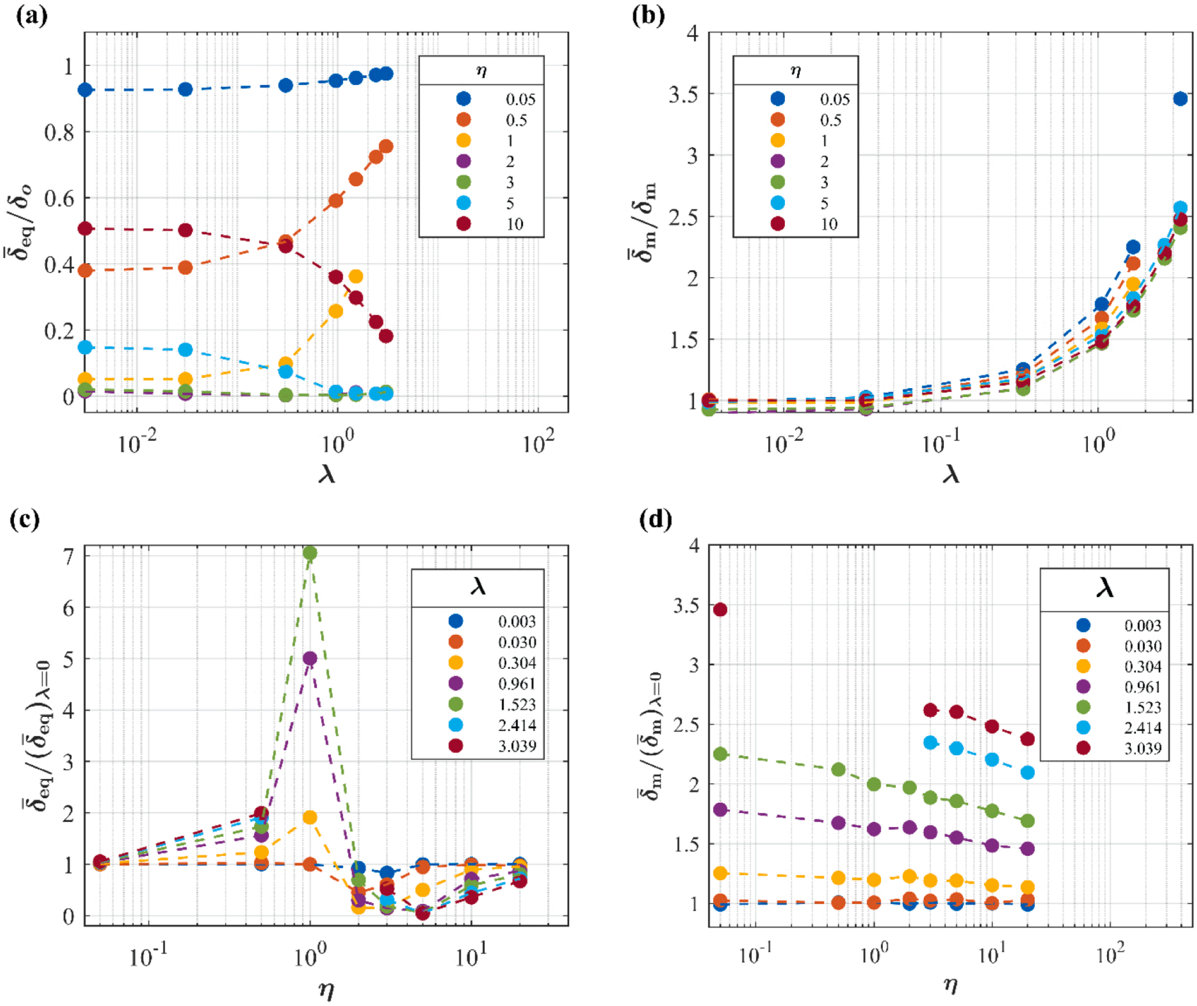

Fig. 12. Effect of elastic deformation on bulk solid with isosceles trapezoidal pattern interface. Compared to intrinsic properties: (a) effective equilibrium separation $\bar{\delta}_{\mathrm{eq}}$ and (b) effective interaction range $\bar{\delta}_{\mathrm{m}}$ as function of λ for varies η. Compared to rigid results: (c) $\bar{\delta}_{\mathrm{eq}}$ and (d) $\bar{\delta}_{\mathrm{m}}$ as function of η for various λ.

top flat segment of the trapezoidal pattern is out of the van der Waals interaction range when the bulk is stiff, but it gets compressed back into the interaction range when the bulk is softer, resulting the interface tractions becoming more non-uniform, hence reducing $\bar{\delta}_{\mathrm{eq}}$. Furthermore, the pattern heights (e.g., $1 < \eta < 5$) that span the majority of the interaction range of the TSR have highly non-uniform tractions across the interface at the equilibirum configuration (see Fig. 10a), i.e., $\min(y^{\mathrm{U}})$ must be vary close to $\max(y^{\mathrm{L}})$ in order to reach $\bar{\delta}_{\mathrm{eq}}$that $\bar{\delta}_{\mathrm{eq}} \ll \delta_{\mathrm{o}}$ (see Fig. 12a, c). One can also see in Fig. 12c that as η increases, $\bar{\delta}_{\mathrm{eq}}$ approaches the rigid result, e.g. $\bar{\delta}_{\mathrm{eq}}/(\bar{\delta}_{\mathrm{eq}})_{\lambda=0} = 1$, for all λ because the dominant interactions are essentially confined to the lower flat segment of the trapezoidal pattern. Lastly, $\bar{\delta}_{\mathrm{m}}$ increases with increasing λ for all η when compared to the intrinsic interaction range, δ_{m}, (Fig. 12b) due to the aforementioned compression and elongation of the surface pattern, and $\bar{\delta}_{\mathrm{m}}$ decreases with increasing of η for all λ when compared to the rigid behaviors (Fig. 12d).

6. Conclusions

Interfaces rarely realize their actual intrinsic adhesion strength due to surface topography and elastic deformation in the adhered bulk materials. For any material system, the intrinsic strength is the upper limit of adhesion such that no interface pattern will achieve higher adhesion than the ideally perfectly flat surfaces, but such ideal surfaces rarely exist. In one notable exception, if edge boundary effects are exploited for fibrillar structures, Gao and Yao (2004) have shown an optimal concave fiber tip geometry can achieve the intrinsic adhesion strength, although sensitivity of adhesion strength to fiber tip geometry decreases as fiber diameter decreases. We have shown that the interplay between *non-conformal* surface geometries and the intrinsic traction-separation behavior leads to highly non-uniform interface fields that depend strongly on the overall separation and control the effective adhesive properties. If the normal separation δ between surfaces of adhered solids is approximately in the $1 \sim 100\,\mathrm{nm}$ range, i.e. the range of surface tractions, complex adhesive interactions arise with varying strength that depend on the intrinsic adhesive properties as well as the bulk material elasticity. If the separation is very small, e.g. in the sub-nanometer range, the strong repulsion that arises depends on that local separation.

We have shown that the interplay between the intrinsic TSR and the interface geometry strongly affects the effective interfacial strength and work of separation, and both tend to decrease non-linearly as the pattern height ratio, an important non-dimensional parameter, $\eta = h_0/\delta_\mathrm{m}$, increases. Three regimes of η are identified: smooth, geometry-sensitive, and asymptotic. The intrinsic adhesion properties are recovered in the smooth regime, and effective adhesion behavior is controllable in the geometry-sensitive regime. In the small η range, a pattern with a diagonal surface, e.g. the trapezoidal interface, has superior adhesion performance, while flat surface patterns perform better in larger η range.

For a given interface geometry, elastic deformation of the bulk solids can significantly distort the surface geometry and alter the interface stress distribution as the two surfaces are adhered and then pulled apart during loading. We have identified another important non-dimensional parameter measured at the maximum intrinsic traction, $\lambda = \sigma_\mathrm{max}/\delta_\mathrm{m}(H/E)^*$, that characterizes the importance of the bulk deformation relative to the interface deformation. For a perfectly flat interface, significant spring-back is observed in the system when $\lambda > 5$, and this tendency also leads to spring back (and numerical problems) for patterned interfaces. For $\lambda > 0.030$, the interface pattern height is flattened at effective equilibrium but elongated at maximum load, and such elastic straining in the patterned region causes load-dependent changes of the interface geometry and, therefore, can strongly influence the effective separation behavior. Generally, as the system becomes more compliant, there is a trade-off that the interface toughness increases while the interfacial strength decreases. For $\lambda \leq 0.030$ or η outside of the elasticity-sensitive regime $0.5 \lesssim \eta \lesssim 30$, the elastic solids can be assumed as rigid to accurately predict the effective interfacial adhesion properties, thus, simplifying calculations for engineering design.

Based upon current understanding, the ability to design surfaces with desired adhesion and toughness is, at best, trial and error, and there are potentially significant opportunities for improvement in many applications. The understanding of adhesion of *non-conformal* interfaces will enable advanced micro- and nano-patterning techniques to be exploited to realize new approaches to control interface adhesion and toughness through geometry, going beyond the traditional approach of controlling adhesion through chemistry. The understanding of the impact of *non-conformally* patterned surface geometry on the separation mechanisms established here can be exploited to realize new materials and mechanical systems with specifically tuned adhesive properties to advance a wide range of technologies. Further investigations are underway, including crack propagation and effects of shear tractions. For periodic patterns, we have found relatively small effects of shear tractions on overall normal separation, which is the loading considered in this paper.

Declaration of Competing Interest

The authors declare no conflict of interest.

Acknowledgements

The support from NSF/CMMI Grant 1761726 is gratefully acknowledged. R.R.Z also acknowledges support by a Department of Education GAANN fellowship grant number P200A160282 to the Department of Mechanical Engineering and Applied Mechanics at the University of Pennsylvania.

Appendix A. The potential and small α approximations for TSR (1)

The term multiplying α in the TSR relation (1) is introduced to account for the strong repulsion when surfaces are brought very close together to suppress unphysical material interpenetration. Let

$$T(\delta) = (1 + \alpha\,\delta_\mathrm{o}\,/\,\delta)\;\widetilde{T}(\delta) \tag{19}$$

where $\widetilde{T}$ is the Rose-Ferrante-Smith traction, and the associated adhesive potential is

$$\widetilde{F}(\delta) = (\psi\,/\,\beta)(\delta + \beta - \delta_0)\exp\left(-\frac{\delta - \delta_\mathrm{o}}{\beta}\right) \tag{20}$$

The potential associated with non-zero α, with $T = -\mathrm{d}F\,/\mathrm{d}\delta$ in (1), is

$$F(\delta) = \widetilde{F}(\delta) + \alpha\frac{\psi\,\delta_\mathrm{o}}{\beta}\left[\exp\left(-\frac{\delta - \delta_\mathrm{o}}{\beta}\right) - \frac{\delta_\mathrm{o}}{\beta}\exp\left(\frac{\delta_\mathrm{o}}{\beta}\right)E_1\left(\frac{\delta_\mathrm{o}}{\beta}\right)\right] \tag{21}$$

where $E_1(x) = \int_x^\infty (e^{-t}\,/t)\,\mathrm{d}t$ is the exponential integral.

For any α, the traction-free equilibrium separation is δ_o. At the end of Section 2, expressions for the maximum traction, the corresponding separation, and the work of separation are given for the case $\alpha = 0$, which is the Rose-Ferrante-Smith TSR. Approximations for the maximum traction and the corresponding separation for small α are given below and let $\widetilde{\delta} = \widetilde{\delta}_\mathrm{m} + \delta_\mathrm{o} = \beta + \delta_\mathrm{o}$ denote the corresponding separation at $\widetilde{\sigma}_\mathrm{max} = \psi\,/(e\beta)$. From (1), expanding $\mathrm{d}T\,/\mathrm{d}\delta = 0$ in terms of $\delta - \widetilde{\delta}$, noting that $\mathrm{d}\widetilde{T}\,/\mathrm{d}\delta = 0$ at $\widetilde{\delta} = \widetilde{\delta}_\mathrm{m} + \delta_\mathrm{o} = \beta$

$+\ \delta_o$, and neglecting higher-order terms (Newton-Raphson approximation) leads to the separation corresponding to the maximum traction

$$\delta_m + \delta_o \simeq \beta + \delta_o - \alpha \frac{\delta_o}{(1+\delta_o/\beta)^2} \tag{22}$$

and from (1)

$$\sigma_{\max} \simeq T\left(\beta + \delta_o - \alpha \frac{\delta_o}{(1+\delta_o/\beta)^2}\right) \tag{23}$$

Appendix B. UMAT implementation and equilibrium iterations

ABAQUS/Standard was used to couple linear static stress analysis with our nonlinear cohesive zone model (1) using implicit integration scheme. Equilibrium iterations are performed at load step until the set of nonlinear equations are solved iteratively using Newton-Raphson method. The bulk material is linear-elastic under 2D plane-strain conditions. Quadratic 4-node quadrilateral elements, CPE4R, with reduced integration as recommended by ABAQUS contact problems were adopted. Note, using quadratic fully integrated elements led essentially to the same results but took longer CPU time. The interface cohesive elements are modeled using the ABAQUS default cohesive element structure but with our user-defined subroutine (UMAT) to describe the interface TSR (1).

In the initial configuration of the model, the upper solid with the trapezoidal pattern is positioned at an arbitrary distance above the rigid flat bottom substrate. The UMAT calculates the normal traction at each integration point of each cohesive element based on its element height, which varies from element to element and with deformation. The height of each cohesive element represents the local separation across the interface. Assigning the appropriate normal traction first to each element is important because the non-uniform interface gap results in a non-uniform interface traction distribution, i.e. each cohesive element has a non-zero stress if its height differs from the intrinsic equilibrium separation, δ_o. The initial configuration is relaxed until $\overline{T} = 0$ corresponding to $\overline{\delta} = \overline{\delta}_{eq}$ and $\overline{v} = 0$ by definition.

In the UMAT, the material Jacobian matrix ($\underline{\underline{J}} = \partial T / \partial \varepsilon$) for the interface constitutive model in (1) must be specified for the Newton-Raphson iterations. An accurate, symmetric Jacobian matrix is required for rapid convergence of the overall equilibrium iterations. However, an incorrect Jacobian matrix will not affect the accuracy of numerical results, but it will just slow down the convergence rate (ABAQUS User's Manual). Since our investigation only involved normal tractions, and to avoid singular matrix, we chose the shear component of the Jacobian matrix to be a small fraction of the normal component, with the off-diagonal components zero, to achieve the highest convergence rate.

Numerical difficulties in cohesive zone models are commonly due to the unstable decay of cohesive tractions as separations increase. Generally, ABAQUS' built in Riks arc-length method and stabilization control are sufficient (Gao and Bower, 2004), but care is required to obtain rapid convergence rate and accurate results. For our problem, the ABAQUS built in Riks arc-length method is needed in the softest case ($\lambda = 3.039$ for $\eta = 3$) to predict the global unstable response of the system due to spring-back tendency. However, finding the correct input values required for the Riks method for a given case is not straightforward, and we found requires a trial-and-error approach.

Another numerical difficulty we found was in computing the effective equilibirum separation $\overline{\delta}_{eq}$ for the cases where the interface geometry gets highly compressed due to increased λ. For the TSR (1), the tangent stiffness of the repulsive traction increases as local separation decreases below δ_o. Therefore, for a low stiffness bulk material, the cohesive elements have relatively high stiffness compared to the bulk material stiffness, thus resulting in numerical convergence difficulties for the nodes shared by the cohesive and the elastic solid elements. While maintaining accurate results, the use of stabilization control helps to resolve such numerical issues (ABAQUS User's Manual; Gao and Bower, 2004).

References

Barthel, E., 2008. Adhesive elastic contacts: JKR and more. J. Phys. D. Appl. Phys. 41 https://doi.org/10.1088/0022-3727/41/16/163001.

Bažant, Z.P., 2001. Concrete fracture models: testing and practice. Eng. Fract. Mech. 69, 165–205. https://doi.org/10.1016/S0013-7944(01)00084-4.

Bradley, R.S., 1932. LXXIX. The cohesive force between solid surfaces and the surface energy of solids. London, Edinburgh, Dublin Philos. Mag. J. Sci. 13, 853–862. https://doi.org/10.1080/14786449209461990.

Ciavarella, M., Greenwood, J.A., Barber, J.R., 2017. Effect of tabor parameter on hysteresis losses during adhesive contact. J. Mech. Phys. Solids 9, 236–244. https://doi.org/10.1016/j.jmps.2016.10.005.

Cordisco, F.A., Zavattieri, P.D., Hector, L.G., Bower, A.F., 2012. Toughness of a patterned interface between two elastically dissimilar solids. Eng. Fract. Mech. 96, 192–208. https://doi.org/10.1016/j.engfracmech.2012.07.018.

Cordisco, F.A., Zavattieri, P.D., Hector, L.G., Carlson, B.E., 2016. Mode i fracture along adhesively bonded sinusoidal interfaces. Int. J. Solids Struct. 83, 45–64. https://doi.org/10.1016/j.ijsolstr.2015.12.028.

Derjaguin, B., 1934. Untersuchungen über die reibung und adhäsion, iv - theorie des anhaftens kleiner teilchen. Kolloid-Zeitschrift 69, 155–164. https://doi.org/10.1007/BF01433225.

Derjaguin, B.V., Muller, V.M., Toporov, Y.P., 1975. Effect of contact deformations on the adhesion of particles. J. Colloid Interface Sci. 53, 314–326. https://doi.org/10.1016/0021-9797(75)90018-1.

Fuller, K., Tabor, D., 1975. The effect of surface roughness on the adhesion of elastic solids. Proc. R. Soc. London. A. Math. Phys. Sci. 345, 327–342. https://doi.org/10.1098/rspa.1975.0138.

Gao, Y.F., Bower, A.F., 2004. A simple technique for avoiding convergence problems in finite element simulations of crack nucleation and growth on cohesive interfaces. Model. Simul. Mater. Sci. Eng. 12, 453–463. https://doi.org/10.1088/0965-0393/12/3/007.

Gao, H., Yao, H., 2004. Shape insensitive optimal adhesion of nanoscale fibrillar structures. Proc. Natl. Acad. Sci. U. S. A. 101, 7851–7856. https://doi.org/10.1073/pnas.0400757101.

Gowrishankar, S., Mei, H., Liechti, K.M., Huang, R., 2012. A comparison of direct and iterative methods for determining traction-separation relations. Int. J. Fract. 177, 109–128. https://doi.org/10.1007/s10704-012-9758-3.

Guo, Z.K., Kobayashi, A.S., Hay, J.C., White, K.W., 1999. Fracture process zone modeling of monolithic Al2O3. Eng. Fract. Mech. 63, 115–129. https://doi.org/10.1016/s0013-7944(99)00030-2.

Hensel, R., Moh, K., Arzt, E., 2018. Engineering micropatterned dry adhesives: from contact theory to handling applications. Adv. Funct. Mater. 28 https://doi.org/10.1002/adfm.201800865.

Hong, S., Kim, K.S., 2003. Extraction of cohesive-zone laws from elastic far-fields of a cohesive crack tip: a field projection method. J. Mech. Phys. Solids 51, 1267–1286. https://doi.org/10.1016/S0022-5096(03)00023-1.

Hosseini, M.S., Cordisco, F.A., Zavattieri, P.D., 2019. Analysis of bioinspired non-interlocking geometrically patterned interfaces under predominant mode I loading. J. Mech. Behav. Biomed. Mater. 96, 244–260. https://doi.org/10.1016/j.jmbbm.2019.04.047.

Hossain, M.Z., Hsueh, C.J., Bourdin, B., Bhattacharya, K., 2014. Effective toughness of heterogeneous media. J. Mech. Phys. Solids 71, 15–32. https://doi.org/10.1016/j.jmps.2014.06.002.

Israelachvili, J.N., 1974. The nature of van der waals forces. Contemp. Phys. 15, 159–178. https://doi.org/10.1080/00107517408210785.

Israelachvili, J.N., 2011. Intermolecular and Surface Forces: Third Edition, Intermolec. Surf. Forces: Third Edition. https://doi.org/10.1016/C2011-0-05119-0.

Israelachvili, J.N., Tabor, D., 1972. The measurement of van der waals dispersion forces in the range 1.5 to 130 nm. Proc. R. Soc. London. A. Math. Phys. Sci. 331, 19–38.

Jeong, H.E., Lee, J.-.K., Kim, H.N., Moon, S.H., Suh, K.Y., 2009. A nontransferring dry adhesive with hierarchical polymer nanohairs. Proc. Natl. Acad. Sci. U. S. A. 106, 5639–5644. https://doi.org/10.1073/pnas.0900323106.

Jiang, L.Y., Huang, Y., Jiang, H., Ravichandran, G., Gao, H., Hwang, K.C., Liu, B., 2006. A cohesive law for carbon nanotube/polymer interfaces based on the van der waals force. J. Mech. Phys. Solids 54, 2436–2452. https://doi.org/10.1016/j.jmps.2006.04.009.

Johnson, K.L., 1985. Contact Mechanics. Cambridge University Press. https://doi.org/10.1017/CBO9781139171731 https://doi.org/.

Johnson, K.L., Greenwood, J.A., Higginson, J.G., 1985. The contact of elastic regular wavy surfaces. Int. J. Mech. Sci 27, 383–396.

Johnson, K.L., Kendall, K., Roberts, A.D., 1971. Surface energy and the contact of elastic solids. Proc. R. Soc. A Math. Phys. Eng. Sci. 324, 301–313. https://doi.org/10.1098/rspa.1971.0141.

Li, Y., Ortiz, C., Boyce, M.C., 2011. Stiffness and strength of suture joints in nature. Phys. Rev. E - Stat. Nonlinear, Soft Matter Phys. https://doi.org/10.1103/PhysRevE.84.062904.

Li, Y., Ortiz, C., Boyce, M.C., 2013. A generalized mechanical model for suture interfaces of arbitrary geometry. J. Mech. Phys. Solids 61, 1144–1167. https://doi.org/10.1016/j.jmps.2012.10.004.

Lin, E., Li, Y., Ortiz, C., Boyce, M.C., 2014. 3D printed, bio-inspired prototypes and analytical models for structured suture interfaces with geometrically-tuned deformation and failure behavior. J. Mech. Phys. Solids 73, 166–182. https://doi.org/10.1016/j.jmps.2014.08.011.

Maugis, D., 2013. Contact, Adhesion and Rupture of Elastic Solids. Springer Science & Business Media.

Menga, N., Afferrante, L., Carbone, G., 2016. International journal of solids and structures adhesive and adhesiveless contact mechanics of elastic layers on slightly wavy rigid substrates. Int. J. Solids Struct. 88–89, 101–109. https://doi.org/10.1016/j.ijsolstr.2016.03.016.

Na, S.R., Sarceno, D.A., Liechti, K.M., 2016. Ultra long-range interactions between silicon surfaces. Int. J. Solids Struct. 80, 18–180.

Needleman, A., 1990. An analysis of tensile decohesion along an interface. J. Mech. Phys. Solids 38, 289–324. https://doi.org/10.1016/0022-5096(90)90001-K.

Park, K., Paulino, G.H., 2011. Cohesive zone models: a critical review of traction-separation relationships across fracture surfaces. Appl. Mech. Rev. 64 https://doi.org/10.1115/1.4023110.

Pastewka, L., Robbins, M.O., 2014. Contact between rough surfaces and a criterion for macroscopic adhesion. Proc. Natl. Acad. Sci. 111, 3298–3303. https://doi.org/10.1073/pnas.1320846111.

Persson, B.N.J., 2014. On the fractal dimension of rough surfaces. Tribol. Lett. https://doi.org/10.1007/s11249-014-0313-4.

Rose, J.H., Ferrante, J., and Smith, J.R., 1981. Universal binding energy curves for metals and bimetallic interfaces 47, 675–678.

Springman, R.M., Bassani, J.L., 2008. Snap transitions in adhesion. J. Mech. Phys. Solids 56, 2358–2380. https://doi.org/10.1016/j.jmps.2007.12.009.

Springman, R.M., Bassani, J.L., 2009. Mechano-chemical coupling in the adhesion of thin-shell structures. J. Mech. Phys. Solids 57, 909–931. https://doi.org/10.1016/j.jmps.2009.02.002.

Tabor, D., Winterton, R.H.S., 1968. Surface forces: direct measuremen of normal and retarded van der waals forces. Nature 219, 1120–1121. https://doi.org/10.1038/220940c0.

Turner, K.T., Spearing, S.M., 2002. Modeling of direct wafer bonding: effect of wafer bow and etch patterns. J. Appl. Phys. https://doi.org/10.1063/1.1521792.

Turner, K.T., Spearing, S.M., 2006. Mechanics of direct wafer bonding. Proc. R. Soc. A Math. Phys. Eng. Sci. https://doi.org/10.1098/rspa.2005.1571.

Tvergaard, V., Hutchinson, J.W., 1993. The influence of plasticity on mixed mode interface toughness. J. Mech. Phys. Solids 41, 1119–1135. https://doi.org/10.1016/0022-5096(93)90057-M.

Tvergaard, V., Hutchinson, J.W., 2009. International journal of solids and structures analyses of crack growth along interface of patterned wafer-level. Cu – Cu bonds 46, 3433–3440. https://doi.org/10.1016/j.ijsolstr.2009.05.015.

Wu, C., Gowrishankar, S., Huang, R., Liechti, K.M., 2016. On determining mixed-mode traction–separation relations for interfaces. Int. J. Fract. 202, 1–19. https://doi.org/10.1007/s10704-016-0128-4.

Wu, C., Huang, R., Liechti, K.M., 2019. Simultaneous extraction of tensile and shear interactions at interfaces. J. Mech. Phys. Solids 125, 225–254. https://doi.org/10.1016/j.jmps.2018.12.004.

Xia, S.M., Ponson, L., Ravichandran, G., Bhattacharya, K., 2013. Adhesion of heterogeneous thin films - I: elastic heterogeneity. J. Mech. Phys. Solids. https://doi.org/10.1016/j.jmps.2012.10.014.

Xia, S.M., Ponson, L., Ravichandran, G., Bhattacharya, K., 2015. Adhesion of heterogeneous thin films II: adhesive heterogeneity. J. Mech. Phys. Solids. https://doi.org/10.1016/j.jmps.2015.06.010.

Xu, X.P., Needleman, A., 1993. Void Nucleation By Inclusion Debonding in a Crystal Matrix. MSMSE.

Zavattieri, P.D., Hector, L.G., Bower, A.F., 2007. Determination of the effective mode-I toughness of a sinusoidal interface between two elastic solids. Int. J. Fract. 145, 167–180. https://doi.org/10.1007/s10704-007-9109-y.